Poiseuille–Rayleigh–Bénard instability of a channel flow with uniform cross-flow and thermal slip

Cite as: Phys. Fluids **33**, 053612 (2021); https://doi.org/10.1063/5.0050006
Submitted: 11 March 2021 . Accepted: 07 May 2021 . Published Online: 26 May 2021

Mohamin B M Khan, Muhammad Sani, Sukhendu Ghosh, and Harekrushna Behera

Physics of Fluids ARTICLE scitation.org/journal/phf

Poiseuille–Rayleigh–Bénard instability of a channel flow with uniform cross-flow and thermal slip

Cite as: Phys. Fluids **33**, 053612 (2021); doi: 10.1063/5.0050006
Submitted: 11 March 2021 · Accepted: 7 May 2021 ·
Published Online: 26 May 2021

Mohamin B M Khan,[1,a)] Muhammad Sani,[1,b)] Sukhendu Ghosh,[2,c)] and Harekrushna Behera[1,d)]

AFFILIATIONS

[1]Department of Mathematics, College of Engineering and Technology, SRM Institute of Science and Technology, Kattankulathur, Chennai, Tamil Nadu 603203, India
[2]Department of Mathematics, Indian Institute of Technology Jodhpur, Rajasthan 342037, India

[a)]Electronic mail: muhyamin77@gmail.com
[b)]Electronic mail: msdjunior9@gmail.com
[c)]Electronic mail: sukhendu.math@gmail.com
[d)]Author to whom correspondence should be addressed: hkb.math@gmail.com

ABSTRACT

Stability characteristics of a pressure-driven Poiseuille type flow are explored in a horizontal channel with porous walls. The flow is modified with a thermal gradient, and the temperature slips alongside a uniform cross-flow for three different configurations: (i) the flow having heat influx/outflux and temperature jump across the channel walls with internal heat generation in the fluid, (ii) the flow with constant wall temperatures (not necessarily equal) and no internal heat source, and (iii) the flow having a temperature jump/slip at the upper wall and lower wall with a constant temperature. The Reynolds, Péclet, and Rayleigh numbers govern the behavior of the thermal and velocity profiles along with the physical aspects of the flow. The modified Orr–Sommerfeld and energy equations are derived for the perturbed system by the normal mode analysis and solved using the Chebyshev collocation method, while the energy budget analysis is used to further illustrate the stability characteristics of the system. The resulting eigenvalues and eigenfunctions are used to analyze the growth rate characteristics, neutral stability ranges, velocity isolines, and temperature isotherms for each flow configuration. Further, the energy from various sources is calculated by making use of eigenfunctions corresponding to the unstable eigenmodes. An increase in the Rayleigh and Reynolds numbers promotes the flow instability; whereas, a higher cross-flow Reynolds number suppresses the instability by raising the upward cross-flow. The porous walls, characterized by the velocity slip and wall shear, inhibit the Poiseuille–Rayleigh–Bénard instability of the system. The higher temperature difference/lower wall temperature and the stronger thermal slip, respectively, destabilize and stabilize the flow. Conclusively, the flow instability varies depending on the configuration.

I. INTRODUCTION

The stability characteristics of shear flows are widely investigated owing to their vast applications in the industry, including aerospace, biomedical, instrumentation, geophysics, polymer, and food processing (Wang,[1] Weisshaar,[2] Criminale, Jackson, and Joslin,[3] etc.). Moreover, the influence of thermal processes on aspects of meteorology and geophysics is evident in the literature, and thermally modified shear flows are prominent in geophysical fluid mechanics, e.g., vertical temperature variations affect the wind flow near the ground, and temperature and salinity variations are highly influential facets in dynamical oceanography.[4] The varied geometrical models are essential for the comprehension of governing characteristics of such flows. The flow geometry discussed in this work can be found in a wide range of industrial applications, e.g., filtration and flow in artificial kidneys are some important processes in the biomedical industry. Further, in cooling–heating applications, the use of moving fluids to transport or remove heat is well known, ranging from the circulation of coolant through a nuclear reactor to the mounting of a power transistor on a block with cooling fins. Similarly, in chemical vapor deposition, hyperporous media in the cooling of electronic equipment, along with in boundary layer control areas, the effect of fluid cross-flow across channels is of great interest.[5]

Such diverse potential applications of shear flow rely on the introduction of targeted modifications to the flow models. In particular, for flows governed by thermal parameters like the temperature slip, the ancillary effects of cross-flow across the channel walls are of

significant interest, especially in microelectronic cooling and passive temperature control.[6] From earlier works of Hains[7] and Sheppard,[8] fluid cross-flow is shown to stabilize the fluid flow in a channel, while Potter and Graber[9] demonstrated the destabilizing effect of a temperature difference across the walls. Accordingly, the present work examines the stability characteristics of the plane Poiseuille flow under different thermal conditions at the porous walls combined with the uniform cross-flow across the channel. Moreover, this investigation aims to elaborate on the influence of temperature difference between walls, wall velocity slip, and thermal boundary slip on the stability of the flow.

The stability of Poiseuille flow, along with other properties, can be maintained using a cross-flow through the layer, with inflow and outflow across the channel walls.[8,10] This modification to the shear flow is applied in the petroleum industry, filtration, purification processes, especially in the transport of species through various flow systems.[11] The model for cross-flow is considered as an injection of a fluid through one wall and suction through the opposite wall in a plane Couette–Poiseuille flow between porous walls leading to a non-parallel flow. The presence of such cross-flow produces a significant increase in the critical Reynolds number.[7] In the flow of a Newtonian fluid between porous walls with a pressure gradient and a uniform cross-flow across the walls, the cross-flow has positive effects on the stability of the channel flow.[5,8] In the plane Couette–Poiseuille flow with a fluid cross-flow, the cross-flow stabilization and Couette stabilization act in a similar manner, with the cause of instability being the resonant interactions of Tollmien–Schlichting waves and at large values of cross-flow Reynolds number stabilization occurs due to decay in energy production.[12] Recently, Bajaj[13] studied the stability characteristics of the plane Poiseuille flow subjected to a uniform cross-flow with constant wall temperature. They deduced that the cross-flow stabilizes or destabilizes the flow depending upon the magnitude and direction.

Furthermore, the Poiseuille flow subjected to a temperature gradient has geophysical and technological applications, like, in the systems involving cooling of the electronic instruments.[14,15] The Benard–Poiseuille flow in a rectangular channel, that is, heated from below results in thermal stratification and convection induced transversal rolls.[16] In a plane Poiseuille flow with thermal stratification, the longitudinal rolls correspond to low Reynold numbers, and Tollmien–Schlichting waves correspond to high Reynolds numbers.[17] The viscous effects under the influence of heat transfer manifest as a skew-symmetric base flow velocity profile in a plane Poiseuille flow, while the thermal gradient across the walls reduces the critical Reynolds number of the flow thereby destabilizing flow across the channel.[9] Viscosity, thermal diffusivity, and buoyancy affect the linear, secondary, and transient growths of the instability in channel flow under the influence of wall heating and cooling.[18] Furthermore, the wall heating destabilizes the fluid flow for low viscosity near channel walls, while the effect on secondary instability is the opposite of that on primary instability.[18] Wall heating is found to stabilize the flow under effects of heat transfer in a low-speed plane Couette–Poiseuille air-flow, while the wall velocity and critical layer locations have a defining role in the stability of the flow.[19] The effect of boundary heating and internal heating on the instability of a Rayleigh–Bènard–Poiseuille flow was examined by Barletta and Nield[20] for nontraveling longitudinal rolls that were independent of Reynolds and Prandtl numbers. Two different Rayleigh numbers were used to characterize the internal heat generation and heating of the isothermal channel walls. Additionally, Nield and Barletta[21] explored a basic Poiseuille throughflow along with internal heat generation in the same manner and focused on the thermo-convective instability.

Application of the thermal gradient to the channel flow, modeled by convective boundary conditions, necessitates the implementation of temperature jump condition that arises due to abrupt change of the molecular structure at the fluid–solid wall interfaces.[22] The practical applications of thermally modified shear flow systems range from the microlevel in electronic devices, heat exchangers, and fuel cells to the macrolevel in passive thermal control and thermal logic components.[6] The subsequent temperature jump condition, analogous to the velocity slip condition, needs a temperature slip across the interface to implement appropriate heat flux conditions.[23] Additionally, the temperature slip and velocity wall slip have also been discussed for a boundary layer flow on a vertical surface,[24] for a stretching surface,[25] and for a nonlinear accelerated flow past cylinders with the wall conditions.[26]

Shear flows and various other complex flow systems like flow systems with asymmetry, varying boundary properties, temperature/concentration stratification, viscosity variation have been solved by the help of collocation methods.[27–29] In recent decades, the Chebyshev spectral collocation method has emerged as the preferred technique to solve hydrodynamic stability problems.[30,31]

In particular, the Orr–Sommerfeld system with modifications and the associated eigenvalue problems are tackled using this method. Pioneering work by Orszag[32] used the Chebyshev polynomials expansions and the matrix *QR* algorithm to solve the Orr–Sommerfeld system. High accuracy was obtained very economically using this technique, and the critical Reynolds number of linear instability for plane Poiseuille flow was evaluated as 5772.22. Additionally, they also elucidated the suitability of Chebyshev polynomials for solving the hydrodynamic stability problems as compared to other kinds of expansions. The Orr–Sommerfeld equation and linearized energy equation can be modified to model pressure-driven flow with viscous heating in a channel.[33] The system was solved by help of the Chebyshev spectral collocation method with the temperature dependence of viscosity governed by Nahme's law, illustrating the destabilizing effect of viscous heating and decrease in critical Reynolds number corresponding to Nahme number.[33] A nonsymmetric mean flow and the presence of cross-flow through the channel walls with Navier-slip condition on the velocity results in a complicated Orr–Sommerfeld analysis, such a system can also be solved for both symmetric and nonsymmetric type slip boundary conditions by the similar collocation method.[12,29]

The aforementioned research works have separately examined instabilities of different Poiseuille type flow configurations including thermal and wall-velocity effects. However, in these investigations, a generalized scenario has not been explored for a realistic physical problem. The present work aims to study a comprehensive problem that includes the combined effects of cross-flow, wall-slip, thermal gradients, and internal heat generation on flow stability in a porous channel. In particular, the present work focuses on the following scenarios: (i) modeling of porous walls using Navier slip condition and investigation of wall slip effects, (ii) inclusion of internal heat source inside the flow field and study of its impact, and (iii) consideration of thermal slip at the walls and discussion of the instability behavior for three different kinds of thermal boundary conditions. Moreover, the energy

budget analysis is presented for these flow configurations, which has not been explored earlier by any researcher. This energy analysis is highly relevant as it allows us to find out the underlying physical mechanisms for the linear instabilities in the considered model.

The present manuscript is arranged as follows: the combination of thermal gradient and cross-flow is applied to the channel in three configurations described in Sec. II: first, with internal heat generated inside the fluid along with heat influx and outflux at the channel walls, second, with constant temperatures at the channel walls, finally, with the lower wall at a constant temperature and the upper wall having a heat outflux. Section II A gives the base velocity and thermal profiles. In Sec. II B, the eigenvalue problem consisting of modified Orr–Sommerfeld and thermal energy equations are derived in the paradigm of linear stability analysis along with the associated boundary conditions. The modified Reynolds–Orr energy equation is derived in Sec. II C. Section III explains the implementation of Chebyshev spectral collocation method for solving the eigenvalue problem along with the convergence study and error analysis. The resulting neutral stability curves, eigenfunctions, and growth rates are examined in Sec. IV to discern the stability characteristics of the system, which is further consolidated using energy budget analysis in Sec. IV A.

II. MATHEMATICAL FORMULATION

A pressure-driven, nonrotating, locally parallel flow of a viscous and incompressible fluid between two infinite porous plates is considered and subjected to a uniform cross-flow and a temperature gradient between the two walls along with internal heat generation. The model is specified using Cartesian coordinates with $x-$ axis in the direction of the flow and $y-$ axis in a perpendicular upward direction. The porous channel walls are at $y = \pm H$, and there is a fluid influx at $y = -H$ and outflux at $y = H$ with constant speed V_0. A constant pressure gradient acts in the streamwise direction and drives the fluid flow with base velocity profile $U_b(y)$, and the temperature gradient between the two walls maintains the mean temperature profile $T_b(y)$ (Fig. 1).

The Navier–Stokes equations of motion with Oberbeck–Boussinesq approximation and an energy equation are used to describe the fluid flow, having the density variations due to the thermal changes and the constant uniform volumetric heat source $\mathcal{Q}$ (see Nield and Barletta[21]) The Oberbeck–Boussinesq approximation model is mechanically incompressible but thermally compressible, and this model is applicable when the density variations are small with pressure and temperature change. In particular, the Boussinesq kind flows are common in nature (for instance, the oceanic circulation, atmospheric fronts), industry (such as dense gas dispersion), and the formed

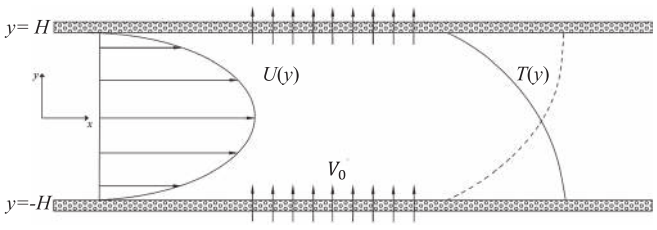

FIG. 1. Schematic of the channel flow system subjected to a uniform cross-flow and temperature gradient.

environment (like central heating). This approximation is known to be accurate for many such flows and makes mathematics and physics simpler.[4] The governing equations for the current model read

$$\nabla.\boldsymbol{q} = 0, \tag{1}$$

$$\partial_t \boldsymbol{q} + (\boldsymbol{q}.\nabla)\boldsymbol{q} = -\frac{\nabla p}{\rho} + \nu\nabla^2 q + g\bar{\alpha}\Delta T\hat{\boldsymbol{j}}, \tag{2}$$

$$\partial_t T + (\boldsymbol{q}.\nabla)T = k_T\nabla^2 T + \frac{\mathcal{Q}}{\rho C_p}, \tag{3}$$

where $\boldsymbol{q} = u\hat{\boldsymbol{i}} + v\hat{\boldsymbol{j}}$ is the fluid velocity vector ($\hat{\boldsymbol{i}}$, $\hat{\boldsymbol{j}}$ are the unit vectors along the coordinate axis), T is the temperature, and $\Delta T = (T - T_w)$ is the temperature difference with respect to a reference temperature T_w (which can change with different flow configurations). Here, $g = 9.81$ m/s^2 is the acceleration due to the gravity, acts vertically downward along the negative y-axis. Moreover, $\bar{\alpha}$ is the thermal expansion coefficient, k_T is the thermal diffusivity, and $\mathcal{Q}$ is the uniform generated heat per unit volume per unit time, while ρ, C_p, p, and t, respectively, denote the density, specific heat, pressure and time, respectively. Additionally, the kinematic viscosity of the fluid is ν ($\nu = \mu/\rho$), where μ is the dynamic viscosity.

Three different scenarios for the flow correspond to disparate sets of the boundary conditions based on cross-flow velocity, wall velocity slip, and temperature variations. The configuration with $\mathcal{Q} > 0$ corresponds to the uniform internal heat generation, which may be caused from a variety of factors such as internal chemical reactions, radioactivity, absorption of thermal radiation, and release of latent heat as water vapor condenses, etc.[4] On the other hand, $\mathcal{Q} < 0$ corresponds to the internal heat demolition. Notably, the Navier-slip velocity condition is used to model the porous wall with small permeability.[29,34] If the wall/boundary of a flow is not perfectly rigid and/or thermally insulated (which includes some hydrocarbons and porous materials, etc.) then in addition to the velocity slip, the system could also have a temperature jump (slip) on the boundary.[6,35,36] Such a thermal slip (due to the temperature jump) at a liquid–solid interface arises due to abrupt molecular changes at the fluid–solid interface and results in temperature slip boundary conditions. This also involves the influence of factors like molecular interactions, lattice formulation of the substrate as well as the molecular structure of the fluid near the wall. The possible uses of the temperature jump/slip are in heat transfer applications such as microcooling for electronic devices, the micro-heat exchangers, and in fuel cells, etc.[6,22] The temperature slip condition is well established in the literature[20–25] and it establishes the relation between the absolute wall temperature and the temperature gradient in the fluid layer near the wall. The set of different boundary conditions is read as

Type-I: The lower and upper walls at $y = \mp H$ act as a heat source and sink, respectively, which is modeled using the thermal slip condition[37,38] and internal heat is generated within the fluid ($\mathcal{Q} \neq 0$). Thus, the realistic boundary conditions (Kuo and Chen[35]) are

$$u = \pm\beta\,\partial_y u, \quad v = V_0 \quad \text{and} \quad T = T_w \pm \lambda\,\partial_y T \text{ at } y = \mp H, \tag{4}$$

where β and λ are the velocity and thermal slip lengths, respectively.

Type-II: The two-channel walls are kept at constant temperatures T_1, T_2 with $T_1 > T_2$ and without internal heat generation (i.e., $\mathcal{Q} = 0$), so that

$$u = \pm\beta\,\partial_y u, \quad v = V_0 \text{ at } y = \mp H \quad \text{and} \quad T = \begin{cases} T_1 & y = -H, \\ T_2 & y = H. \end{cases} \tag{5}$$

Type-III: In this case, the lower channel wall is at constant temperature and the upper wall is freely conducting to the surroundings without internal heat generation ($\mathcal{Q} = 0$). Note that, there can be temperature slip for one wall and not for the other wall, if the walls of the channel are made of different materials. Moreover, this can be a possible configuration for the flow system where one boundary is adiabatic and kept in a constant temperature, but the other boundary is not purely thermally insulated. Thus, the following boundary conditions can be used:

$$u = \pm\beta\,\partial_y u, \quad v = V_0 \text{ at } y = \mp H \quad \text{and}$$
$$\mathrm{T} = \begin{cases} T_0 & y = -H, \\ T_w - \lambda\,\partial_y T & y = H. \end{cases} \tag{6}$$

The above system of governing equations is nondimensionalized based on characteristic length H, characteristic velocity u_m which is the maximum velocity inside the flow domain, along with other scales. The nondimensional quantities denoted with the over tilde ($\tilde{}$) are scaled as follows:

$$(\tilde{x}, \tilde{y}) = \left(\frac{x}{H}, \frac{y}{H}\right), \quad (\tilde{u}, \tilde{v}) = \left(\frac{u}{u_m}, \frac{v}{u_m}\right), \quad \tilde{V}_0 = \frac{V_0}{u_m},$$
$$\tilde{\nabla} = H\nabla, \quad \tilde{t} = \frac{t}{(H/u_m)}, \quad \tilde{p} = \frac{p}{(\mu u_m/H)}, \tag{7}$$
$$\tilde{T} = \frac{T - T_w}{(\nu u_m/g\bar{\alpha}H^2)}, \quad \tilde{\beta} = \frac{\beta}{H}, \quad \tilde{\lambda} = \frac{\lambda}{H}.$$

The set of dimensionless flow parameters, namely, two different Reynolds and Péclet numbers based on maximum velocity u_m and cross-flow velocity V_0, and the Rayleigh number characterizing internal heat ($\mathcal{Q}$) are deduced as

$$Re = \frac{u_m H}{\nu}, \quad r_e = \frac{V_0 H}{\nu}, \quad Pe = \frac{u_m H}{k_T}, \quad p_e = \frac{V_0 H}{k_T} = r_e \frac{Pe}{Re},$$
$$\text{and} \quad Ra = \frac{Pe\, g\bar{\alpha}H^3\mathcal{Q}}{\nu u_m^2 \rho c}. \tag{8}$$

Following Sheppard[8] and Potter and Graber,[9] the resulting nondimensional system of equations [suppressing the over tilde ($\tilde{}$) notation] are

$$\partial_x u + \partial_y v = 0, \tag{9}$$
$$Re(\partial_t u + u\partial_x u + v\partial_y u) = -\partial_x p + \nabla^2 u, \tag{10}$$
$$Re(\partial_t v + u\partial_x v + v\partial_y v) = -\partial_y p + \nabla^2 v + T, \tag{11}$$
$$Pe(T_t + u\partial_x T + v\partial_y T) = \nabla^2 T + Ra, \tag{12}$$

along with the boundary conditions for the three cases Eqs. (4)–(6) that are transformed as following:

$$\textbf{Type I}: \; u = \mp\beta\,\partial_y u; \quad v = V_0 \quad \text{at} \quad y = \pm 1, \quad T = \mp\lambda\partial_y T, \quad y = \pm 1, \tag{13}$$

$$\textbf{Type II}: \; u = \mp\beta\,\partial_y u, \quad v = V_0 \quad \text{at} \quad y = \pm 1, \quad T = T_2 \quad \text{at} \quad y = 1, \quad T = T_1 \quad \text{at} \quad y = -1, \tag{14}$$

$$\textbf{Type III}: \; u = \mp\beta\,\partial_y u, \quad v = V_0 \text{ at } y = \pm 1, \quad T = -\lambda\partial_y T \text{ at } y = 1; \quad T = T_0 \text{ at } y = -1, \tag{15}$$

where the parameters β, λ are, respectively, the nondimensional velocity and thermal slips. In the current formulation, the rates of momentum and heat dissipation are considered equal throughout the fluid flow inside the channel. This corresponds to equality of Reynolds and Péclet numbers, i.e., $Re = Pe$, which further implies $p_e = r_e$ [Eq. (8)]. Thus, the effective parameters governing the models are Re, r_e, and Ra.

A. Mean parallel flow

The hydrodynamic instability of the flow system is analyzed as the evolution of perturbations with respect to the mean/base flow. Following the hydrodynamic stability theory to derive the laminar base/equilibrium flow profile of the flow system, we use the steady, unidirectional, locally parallel flow assumptions.[3,4,8,12,17,30] Under these assumptions, the initial flow is fully developed and unaltered in the streamwise direction. Moreover, it is a flow in the $x-$ direction, that only depends on the wall-normal direction y. Using the base velocity variable $U = (U_b(y), V_0)$ of the flow in the Navier–Stokes equations (9)–(12) and the fact that derivatives with respect to x and t are zero, one can easily derive the base flow equations (see the Appendix).

Further, using the velocity boundary conditions, the following expression of the streamwise base velocity (U_b) is obtained:

$$U_b(y) = \frac{P_0}{r_e}(A + Be^{r_e y} + y), \tag{16}$$

where A and B are given by

$$A = -(1+\beta)\left(\frac{(1 - r_e\beta)e^{-r_e} + (1 + r_e\beta)e^{r_e}}{(1 - r_e\beta)e^{-r_e} - (1 + r_e\beta)e^{r_e}}\right),$$
$$B = 2(1+\beta)\left(\frac{1}{(1 - r_e\beta)e^{-r_e} - (1 + r_e\beta)e^{r_e}}\right).$$

The variation of U_b as a function of y is shown in Fig. 2. Notice that, on introduction of a cross-flow, the base flow profile becomes asymmetric, necessitating the consideration of complete domain for the analysis, unlike a symmetric flow with half domain analysis. Further, by assumption, the cross-stream (y directional) base velocity is much weaker than the streamwise base velocity (U_b) and independent of space and time variables. According to the formulation, the porous channel walls are at $y = \pm H$, and there is a fluid influx at $y = -H$ and outflux at $y = H$ with constant speed V_0. Moreover, the model for cross-flow is considered as an injection of a fluid via the lower wall and suction through the upper wall. It is assumed that the cross-flow/transpiration velocity V_0 is constant and uniform to make the mathematical model equable and simpler. Such a uniform cross-flow along with a streamwise pressure gradient is practically achievable.[39] In conformity with the study by Vadi and Rizvi,[39] "a uniform transmembrane pressure cross-flow microfiltration system is able to maintain uniform transmembrane pressure with high cross-flow velocity and improves the utilization of available filtration area." A different generic concept for achieving a uniform cross-flow over a

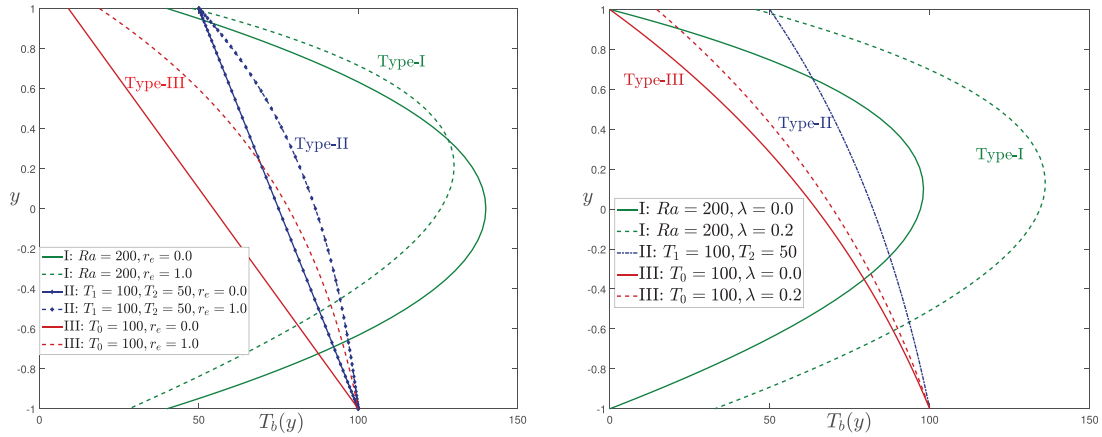

(a) (b)

FIG. 2. Mean velocity profile (U_b) depicted for varying (a) cross-flow Reynolds number(r_e) with $\beta = 0.0$ and (b) velocity slip parameter (β) with $r_e = 2.0$.

porous-walled channel consists of the injection of the fluid via a secondary channel abaft one of the porous walls, which has a linearly converging geometry.[12] Therefore, the formulation of this study can be well valid for the case where both the walls of the porous channel are made of the same material, and if the inflow and outflow pressures are maintained equally. Besides, the parameters range for this investigation are considered in such a way that the approximation holds good and a target appears achievable.

Moreover, the base temperature profile $T_b(y)$ across the flow domain is given by

$$T_b(y) = A_T + B_T e^{r_e y} + C_T y, \tag{17}$$

where A_T, B_T, and C_T are evaluated when Eq. (17) is subjected to the boundary conditions (13)–(15), giving the following thermal profiles.

Type-I: The lower wall at $y = -1$ acts as a heat source and the upper wall at $y = 1$ acts as a heat sink and internal heat is generated within the fluid, i.e., $Ra \neq 0$. The coefficients of the temperature profile Eq. (17) are derived using Eq. (13) as

$$A_T = -\frac{Ra(1+\lambda)}{r_e}\left(\frac{(1-r_e\lambda)e^{-r_e} + (1+r_e\lambda)e^{r_e}}{(1-r_e\lambda)e^{-r_e} - (1+r_e\lambda)e^{r_e}}\right),$$
$$B_T = \frac{2Ra(1+\lambda)}{r_e}\left(\frac{1}{(1-r_e\lambda)e^{-r_e} - (1+r_e\lambda)e^{r_e}}\right) \quad \text{and} \quad C_T = \frac{Ra}{r_e}. \tag{18}$$

Type-II: The two walls at $y = \pm 1$ are kept at constant temperatures T_1, T_2 with $T_1 > T_2$, and without internal heat, i.e., $Ra = 0$. Here, coefficients of the temperature profile Eq. (17) are derived using Eq. (14) as

$$A_T = \frac{1}{2}\operatorname{cosech}(r_e)(T_1 - T_2)e^{r_e},$$
$$B_T = \frac{1}{2}\operatorname{cosech}(r_e)(T_2 - T_1) \quad \text{and} \quad C_T = 0. \tag{19}$$

Type-III: The lower wall is at temperature $T = T_0$ and the upper wall at $y = 1$ is freely conducting to the surroundings, the temperature is approximated by $T(1) = -\lambda\partial_y T(1)$ and no internal heat source (i.e., $Ra = 0$). Here, coefficients of the temperature profile Eq. (17) are derived using Eq. (15) as

$$A_T = \frac{-T_0(1+\lambda r_e)e^{r_e}}{e^{-r_e} - (1+\lambda r_e)e^{r_e}}, \quad B_T = \frac{T_0}{e^{-r_e} - (1+\lambda r_e)e^{r_e}} \quad \text{and} \quad C_T = 0. \tag{20}$$

Figure 3 illustrates the base temperature profile of the above three cases, along with the effects of cross-flow and thermal slip parameters. Temperature profiles are generally parabolic, except for the case for which both walls are at a constant temperature in the absence of cross-flow. An increase in the cross-flow velocity increases the skewness of temperature profile [Fig. 3(a)] as well, while an increase in the temperature slip right shifts the temperature profiles at the nonconstant end of the flow [Fig. 3(b)].

B. Linear stability analysis

The linear stability process uses perturbation analysis in order to test whether or not the equilibrium/base flow is unstable.[9,30,33] Consequently, the base flow variables depend only on wall-normal coordinate y, but the perturbations are usually the function of all independent variables x, y, and t. Instability of the base flow profiles [Eqs. (16) and (17)] is analyzed using the normal mode approach, in which the mean parallel flow is modified with the two-dimensional infinitesimal perturbations parallel/proportional to the waves $e^{i\alpha(x-ct)}$, where $i \equiv \sqrt{-1}$, α is wavenumber in the streamwise direction, and $c = c_r + ic_i$ is the complex wave speed. The linear stability characteristics of the perturbation waves are tracked by checking the exponential time growth/decay of the perturbations. The variables of the perturbed flow are rewritten as (applying the standard normal mode technique to the base velocity, and temperature)

$$[u(y), v(y), T(y)] = \left[U_b(y) + \hat{u}(x,y,t), V_0 + \hat{v}(x,y,t), T_b(y) + \hat{T}(x,y,t)\right], \tag{21}$$

where the perturbations are $(\hat{u}, \hat{v}, \hat{T}) = ((\varphi'(y), -i\alpha\varphi(y), \Theta(y))e^{i\alpha(x-ct)})$. The velocity perturbations are expressed in terms of

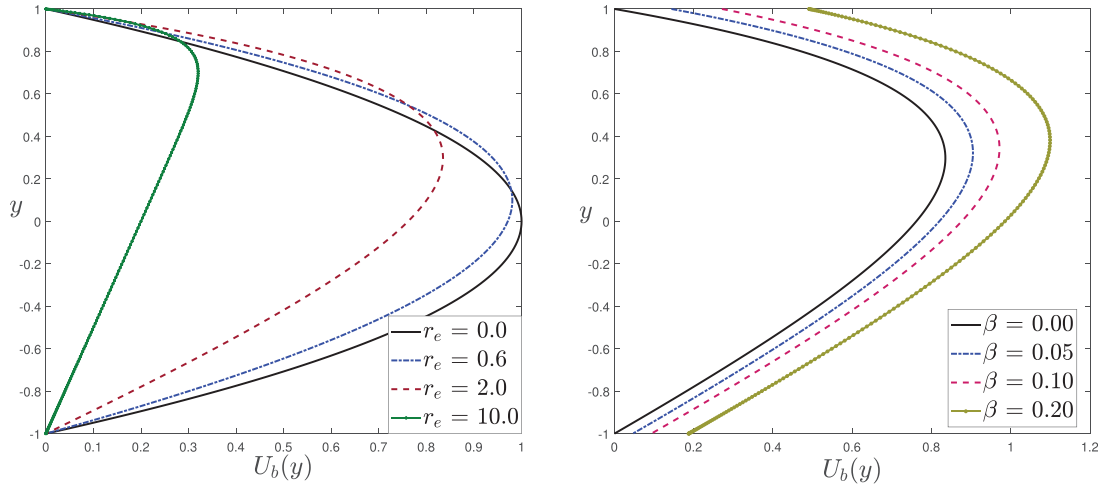

FIG. 3. Base temperature (T_b) profiles for Types-I, II and III with varying (a) cross-flow Reynolds number (r_e) and (b) thermal slip parameter (λ).

the stream function perturbation (φ) and the symbol $' \equiv \frac{d}{dy}$. The temporal frequency of the two-dimensional disturbances is defined by $\omega = \omega_r + i\omega_i = \alpha c$ and the flow will be temporally stable if $\mathrm{Im}(\omega) = \omega_i < 0$, unstable if $\mathrm{Im}(\omega) = \omega_i > 0$, and neutrally stable if $\mathrm{Im}(\omega) = \omega_i = 0$. Consequently, the modified Orr–Sommerfeld and energy equations are derived and given by the following:

$$\varphi'''' - 2\alpha^2\varphi'' + \alpha^4\varphi - r_e(\varphi''' - \alpha^2\varphi') - i\alpha\Theta + i\alpha ReU_b''\varphi = i\alpha Re(U_b - c)(\varphi'' - \alpha^2\varphi), \quad (22)$$

$$\Theta'' - \alpha^2\Theta - r_e\Theta' + i\alpha PeT_b'\varphi = i\alpha Pe(U_b - c)\Theta. \quad (23)$$

The boundary conditions [Eqs. (13)–(15)] are re-framed accordingly as

$$\textbf{Type} - \textbf{I}: \ \varphi = 0, \quad \varphi' \pm \beta\varphi'' = 0 \quad \text{at} \quad y = \pm 1; \quad \Theta \pm \lambda\Theta' = 0 \quad \text{at} \quad y = \pm 1, \quad (24)$$

$$\textbf{Type} - \textbf{II}: \ \varphi = 0, \quad \varphi' \pm \beta\varphi'' = 0 \quad \text{at} \quad y = \pm 1, \quad \Theta = 0 \quad \text{at} \quad y = \pm 1, \quad (25)$$

$$\textbf{Type} - \textbf{III}: \ \varphi = 0, \quad \varphi' \pm \beta\varphi'' = 0 \quad \text{at} \quad y = \pm 1, \quad \Theta + \lambda\Theta' = 0 \quad \text{at} \quad y = 1, \quad \Theta = 0 \quad \text{at} \quad y = -1. \quad (26)$$

The numerical solution of this system is explained in Sec. III along with the convergence and error analysis of the method. Section IV discusses the eigenvalue analysis of the perturbed system and growth rates of the unstable modes calculated using a developed MATLAB code. The following derivation of the generalized kinetic energy equation describes the growth of small disturbances with time in the fluid.

C. Disturbance energy Equation

Generally, an unstable flow implies that the small initial disturbances grow over time in terms of the rate of change of kinetic energy (Schmid, Henningson, and Jankowski,[30] Kelly *et al.*,[40] Ren and Xia[41]) Although the base fluid flow supplies most of the energies for instabilities, the associated energy transfer mechanisms are better understood with the modified energy equation. Following is a concise derivation of the disturbance energy equation for the considered flow model.

The modified Reynolds–Orr energy equation for the disturbed flow is derived from the linearized perturbation equations. The equations obtained by taking the inner product of the perturbed momentum equations in $x, y-$ directions with the velocity perturbations $(\hat{u}, \hat{v})$ are simplified to be interpreted as some sort of energy variation similar to Boomkamp and Miesen[42] and it is deduced that

$$Re\left(\frac{1}{2}\frac{\partial}{\partial t}(\hat{u}^2 + \hat{v}^2) + \frac{U_b}{2}\frac{\partial}{\partial x}(\hat{u}^2 + \hat{v}^2)\right) = \frac{r_e}{2}\frac{\partial}{\partial y}(\hat{u}^2 + \hat{v}^2) - ReU_b'\hat{u}\hat{v} - (\hat{u}\hat{p}_x + \hat{v}\hat{p}_y) - (\hat{u}_x^2 + \hat{v}_x^2 + \hat{u}_y^2 + \hat{v}_y^2) + \frac{\partial}{\partial x}(\hat{u}\hat{u}_x + \hat{v}\hat{v}_x) + \frac{\partial}{\partial y}(\hat{u}\hat{u}_y + \hat{v}\hat{v}_y) + \hat{v}\hat{T}. \quad (27)$$

The resultant equation is averaged with the wavelength (ζ) and integrated over a control volume. Using Gauss divergence theorem and the decomposition of the localized perturbations into their Fourier components, the integrals are simplified, the modified Reynolds–Orr energy equation is derived as

$$\frac{Re}{2\zeta}\frac{\partial}{\partial t}\int_{-1}^{1}\int_{0}^{\zeta}(\hat{u}^2 + \hat{v}^2)dx\,dy = -\frac{\beta^2 r_e}{4\zeta}\frac{\partial}{\partial y}\int_0^{\zeta}\hat{u}_y^2\Big|_{y=-1}^{y=1}dx - \frac{Re}{\zeta}\int_{-1}^{1}\int_0^{\zeta}U_b'\hat{u}\hat{v}\,dx\,dy + \frac{1}{\zeta}\int_{-1}^{1}\int_0^{\zeta}\hat{v}\hat{T}\,dx\,dy - \frac{1}{\zeta}\int_{-1}^{1}\int_0^{\zeta}(\hat{u}_x^2 + \hat{v}_x^2 + \hat{u}_y^2 + \hat{v}_y^2)\,dx\,dy + \frac{\beta}{\zeta}\int_0^{\zeta}\Big((\hat{u}^2 + \hat{u}_y\hat{v}_x)|_{y=-1} + (\hat{u}^2 + \hat{u}_y\hat{v}_x)|_{y=1}\Big)dx. \quad (28)$$

Upon applying normal mode solutions to the above equation, the disturbance energy balance can be decomposed into different terms as follows:

$$DKE^* = BReS^* + CReS^* + VDE^* + TIE^*, \tag{29}$$

where $DKE^* = \frac{\omega_i}{2}\int_{-1}^{1}(|\varphi'|^2 + \alpha^2|\varphi|)dy$ is the mutation rate of disturbance kinetic energy, $BReS^* = -\frac{i\alpha}{4}\int_{-1}^{1} U_b'(\varphi'\bar{\varphi} - \overline{\varphi'}\varphi)dy$ is the Reynolds stress term for energy transformation from the baseflow, $CReS^* = -\frac{\beta^2 r_e}{4Re}\left(|\varphi'|^2|_{y=1} - |\varphi'|^2|_{y=-1}\right)dy$ is the energy contribution due to the cross-flow, $VDE^* = -\frac{1}{2Re}\int_{-1}^{1}(|\varphi''|^2 + 2\alpha^2|\varphi'|^2 + \alpha^4|\varphi|^2)dy + \frac{\beta}{2Re}\left(|\varphi'|^2|_{y=1} + |\varphi'|^2|_{y=-1}\right) + \frac{\alpha^2\beta}{4Re}\left((\overline{\varphi''}\varphi + \varphi''\bar{\varphi})|_{y=1} + (\overline{\varphi''}\varphi + \varphi''\bar{\varphi})|_{y=-1}\right)$ is the viscous dissipation energy in the disturbed flow, and $TIE^* = -\frac{i\alpha}{4Re} \times \int_{-1}^{1}(\varphi\bar{\Theta} - \bar{\varphi}\Theta)dy$ corresponds to the thermally induced energy.

It is worth noticing that Eq. (29), not only contains the classical terms (DKE^*, VDE^*, $BReS^*$) of the Reynolds–Orr energy balance equation for a plane Poiseuille flow with velocity slip,[41] its also modified to incorporate the influence of cross-flow across the channel walls as well as the thermally induced effects ($CReS^*$, TIE^*) in the energy fluctuation. Besides, the rate of change of kinetic energy ($DKE*$) is proportional to the temporal growth rate. Moreover, the dependence of energy balance on velocity slip β is explicit in $CReS^*$, VDE^* and implicit for other terms, while the thermal slip λ has implicit influence on the energy balance via the eigenfunctions φ and Θ. Finally, Eq. (29) is normalized using $I = \frac{1}{2}\int_{-1}^{1}(|\varphi'|^2 + \alpha^2|\varphi|)dy$ to acquire the scaled growth rate $\omega_i = DKE = DKE^*/I$ as

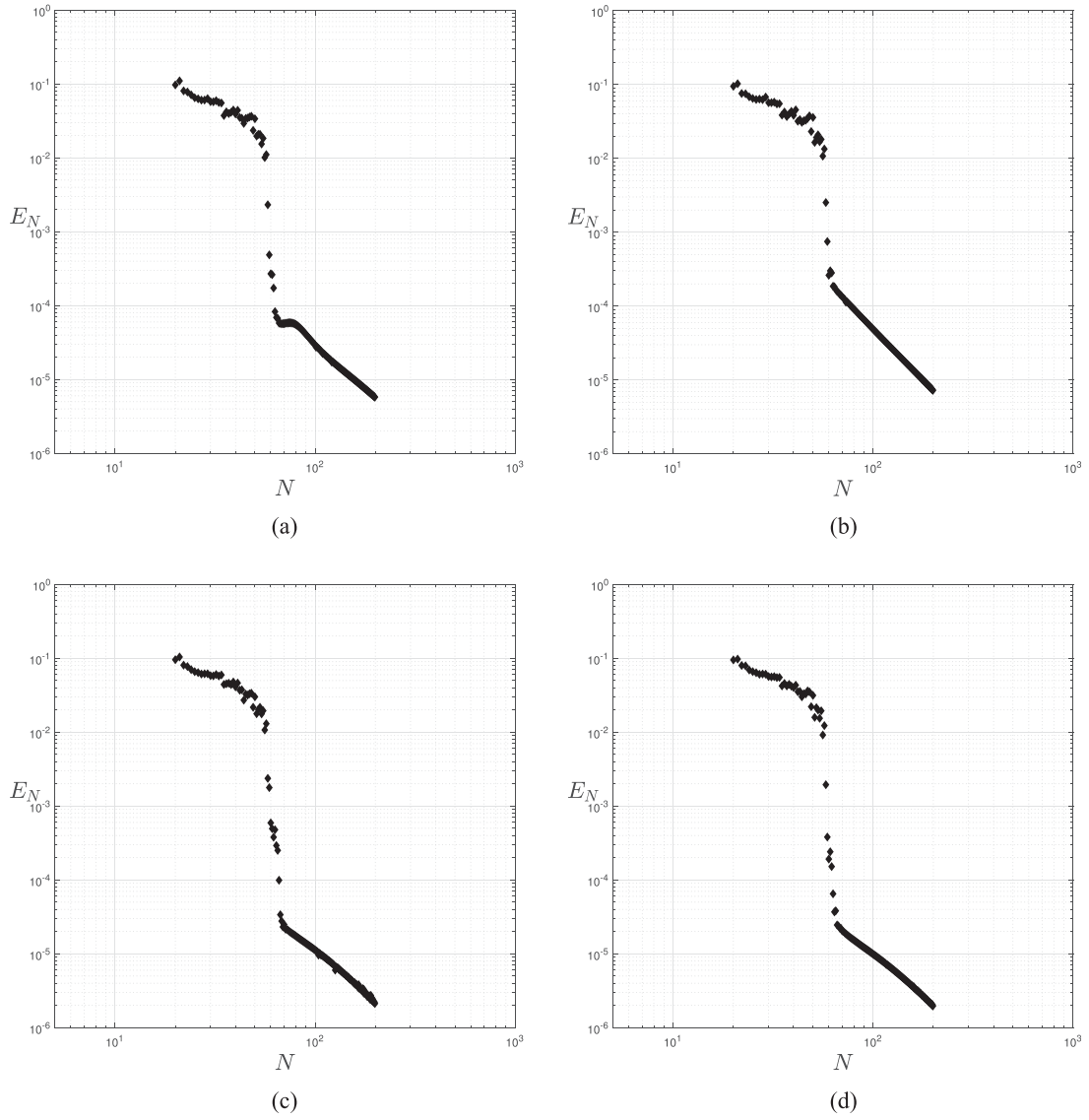

FIG. 4. Relative error E_N against the truncation number N for the Chebyshev polynomials in the case of configurations (a) Type-I with $Ra = 50$, $Re = 10\,000$, $r_e = 0.4$, $k = 1$, $\beta = 0.005$, and $\lambda = 0.2$, (b) Type-I with $Ra = 100$, $Re = 10\,000$, $r_e = 0.4$, $k = 1$, $\beta = 0.005$, and $\lambda = 0.2$, (c) Type-II with $Re = 10\,000$, $r_e = 0.4$, $k = 1$, $T_1 = 100$, $T_2 = 50$, and $\beta = 0.005$, and (d) Type-III with $Re = 10\,000$, $r_e = 0.4$, $k = 1$, $\beta = 0.005$, $T_1 = 100$ and $\lambda = 0.2$. (a) Type-I, $Ra = 50$. (b) Type-I, $Ra = 100$. (c) Type-II. (d) Type-III.

$$DKE = BReS + CReS + VDE + TIE. \tag{30}$$

III. NUMERICAL METHOD AND VALIDATION

The derived modified Orr–Sommerfeld and energy equations form a coupled system, along with the associated boundary conditions, that is, solved using the Chebyshev spectral collocation method.[30,31] First, the system of equations (22) and (23) is written as a generalized eigenvalue problem of the form,

$$\mathcal{A}\boldsymbol{X} = c\mathcal{B}\boldsymbol{X}, \tag{31}$$

where $\boldsymbol{X} = [\varphi\ \Theta]^T$ is the eigenvector corresponding to the eigenvalue c that represents the complex wave speed. The elements of the matrices $\mathcal{A}$ and $\mathcal{B}$ are differential operators which reads

$$\mathcal{A} = \begin{bmatrix} A_{11} & A_{12} \\ A_{21} & A_{22} \end{bmatrix}, \quad \mathcal{B} = \begin{bmatrix} B_{11} & \mathrm{O} \\ \mathrm{O} & B_{22} \end{bmatrix}, \tag{32}$$

where $A_{11} = D^4 - 2\alpha^2 D^2 + \alpha^4 - r_e(D^3 - \alpha^2 D) + \mathrm{i}\alpha ReU_b'' - \mathrm{i}\alpha ReU_b(D^2 - \alpha^2)$, $A_{12} = -\mathrm{i}\alpha$, $A_{21} = -\mathrm{i}\alpha PeT_b'$, $A_{22} = (D^2 - \alpha^2) - r_e D - \mathrm{i}\alpha PeU_b$, $B_{11} = -\mathrm{i}\alpha Re(D^2 - \alpha^2 D)$, $B_{22} = -\mathrm{i}\alpha PeD$, $D^k = d^k/dy^k$, and O is the null operator. Since the eigenvalue problem consists of fourth- and second-order ordinary differential equations (ODEs), the system becomes complete by including six associated boundary conditions corresponding to different flow configurations [Eqs. (24)–(26)]. Next, the Chebyshev spectral collocation method is used to reframe the eigenvalue problem as a system of equations. The perturbation amplitude functions φ and Θ are expanded as the finite sums using Chebyshev polynomials $T_i(y)$ as the basis functions defined over $[-1, 1]$ and satisfying the orthogonality property. The $N-$ truncated series is given by

$$\varphi = \sum_{i=0}^{N} \varphi_i T_i(y), \quad \Theta = \sum_{i=0}^{N} \Theta_i T_i(y), \tag{33}$$

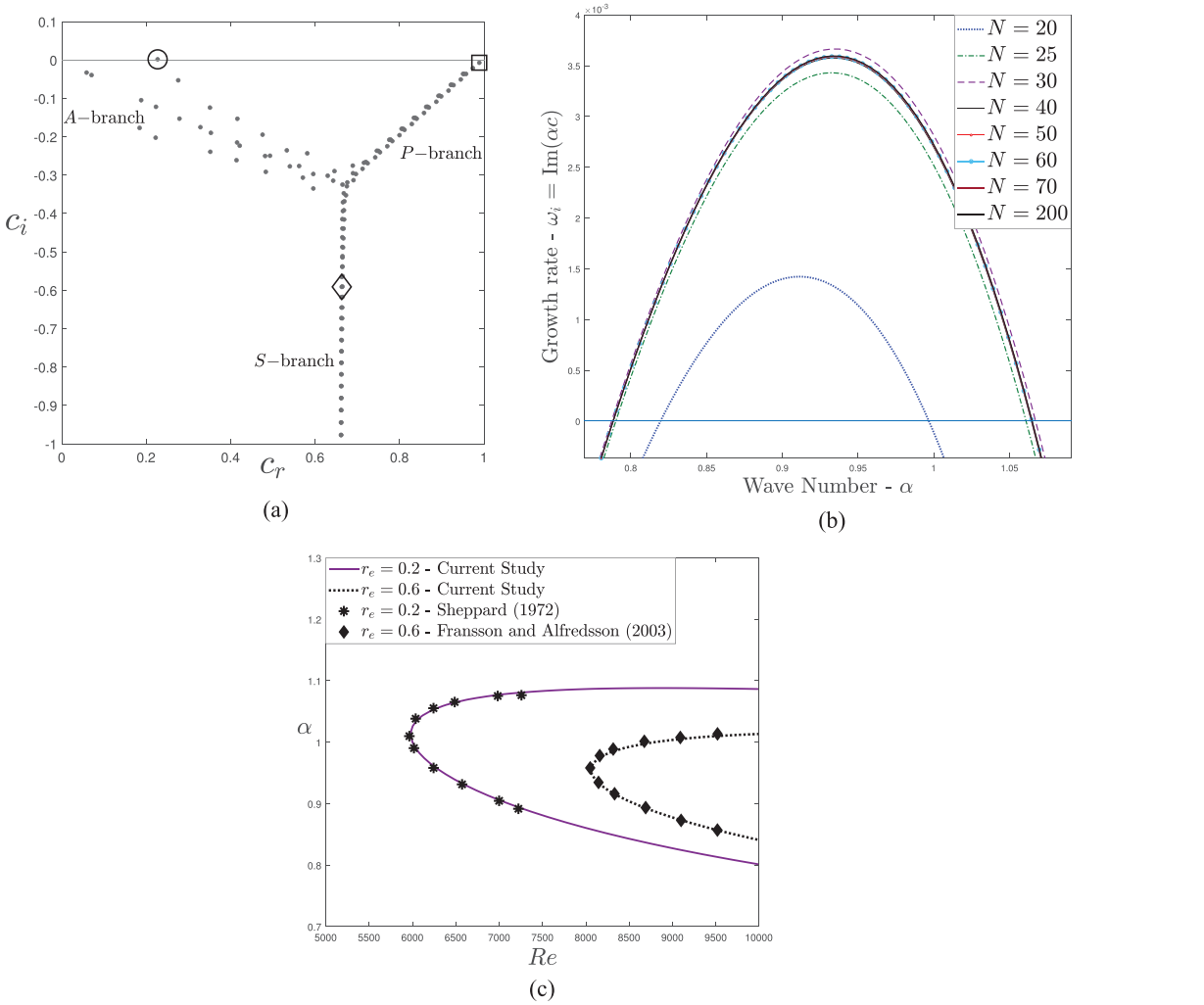

FIG. 5. (a) Eigenvalue Spectrum and (b) Convergence of dispersion curves for Type-I configuration, when $Re = 10\,000$, $Ra = 100$, $r_e = 0.4$ and $\lambda = 0.2$, where the growth rate curves overlap for the values $N > 70$; (c) Neutral stability curves in $Re - \alpha$ plane validating the Type-II configuration in the current study with that of Sheppard[8] and Fransson and Alfredsson,[5] using $T_1 = T_2 = 0$, $\beta = 0$ and $Ra = 0$.

where φ_i and Θ_i are the unknown coefficients. The flow domain is discretized using the extrema of Chebyshev polynomials, known as Gauss–Lobatto collocation points $y_j = \cos(\pi j/N), j \in \{0, 1, 2, \ldots, N\}$, and the functions are evaluated at those points. After implementing Eq. (33) in Eq. (31), the resulting form of the eigenvalue problem is then solved using the well established QZ algorithm (Canuto *et al.*[31]) to evaluate the eigenvalues. Note that, the boundary conditions at upper and lower walls are implemented in Eq. (31) as the top and bottom rows after replacing the corresponding rows in the matrices $\mathcal{A}$ and $\mathcal{B}$. Using the QZ algorithm the matrices $\mathcal{A}$ and $\mathcal{B}$ are recast into the upper triangular forms and the resulting eigenvalues are computed, as the ratio of diagonal elements corresponding to the modified $\mathcal{A}$ and $\mathcal{B}$. However, the accuracy of numerical computation depends on the number of collocation points N.

In this regard, to check the accuracy of numerical computation and convergence of eigenspectrum for different values of N, we have followed the methodology of Tilton and Cortelezzi,[43] and Samanta.[44] For a given N, the relative error (E_N) is defined using the L^2 norm $(||.||_2)$

$$E_N = \frac{||c_{N+1} - c_N||_2}{||c_N||_2}, \tag{34}$$

where the components of the vectors c_N and c_{N+1} are the eigenvalues related to the twenty least stable disturbance modes of the eigenvalue problem Eq. (31), obtained using N and $N+1$ Chebyshev polynomials, respectively. Figures 4(a)–4(d) illustrate the behavior of relative error against the number of Chebyshev collocation points (N) for the three different types of thermal boundary conditions. It is seen that generally for $N \geq 70$ the relative error decreases exponentially beyond the order 10^{-4}, thereby confirming the convergence of the method for the given models. Moreover, since the system has uniform dimensions between the walls, any increase in the value of N increases the number of Gauss–Lobatto collocation points and subsequently the order of accuracy of the solution. However, high N values result in higher computation times as well. Additionally, for higher Rayleigh numbers, the relative error increases [Figs. 4(a) and 4(b)] and higher N may be required for satisfying the needed error tolerance. Thus, the above graphs illustrate that for $N \geq 70$, increasingly accurate numerical results are to be expected with minimal computational costs.

Figure 5(a) illustrates the eigenvalue spectrum for the system of Orr–Sommerfeld and energy equations modeling the porous (less permeable) channel flow with the inclusion of internal heat generation, heat flux across the walls, and a uniform cross-flow. The familiar "Y" shaped spectrum corresponding to the wall-bounded Poiseuille type flow is obtained, having different branches, and following the classification of Mack,[45] the branches are named as $A(c_r \to 0), P(c_r \to 1)$, and $S(c_r \approx 2/3)$. According to Mack,[45] the eigenvalues have been classed based on arranging the eigenvalues in order of decreasing c_i and the range of c_r. The number of eigenvalues on each branch depends on the model as well as the parameter values. Moreover, the unstable mode is located on branch A and the S modes are highly damped. Figure 5(c) compares the neutral stability curves generated from the current computation to the results with those in Sheppard,[8] Fransson, and Alfredsson.[5] The limiting results are obtained by considering no-slip conditions at the walls and $T_1 = T_2 = 0$, for Type-II configuration. It is clearly seen that the current results are in good agreement with those of the earlier works, thus establishing the correctness and validity of the developed numerical code.

The convergence of the Chebyshev spectral collocation method is further demonstrated in Fig. 5(b). The growth rate curves are plotted for the Type-I boundary condition with $Re = 10\,000$, $r_e = 0.4$, $Ra = 100$, $\beta = 0.005$, and $\lambda = 0.2$. It is observed that the dispersion curves overlap and converge for the number of Chebyshev points $N > 70$. In subsequent figures, $N = 100$ is used to generate the dispersion curves, and the desired accuracy is achieved.

IV. RESULTS AND DISCUSSION

The results corresponding to the temporal linear instability of the system are discussed for three different cases with the boundary conditions imposed for the velocity and temperature

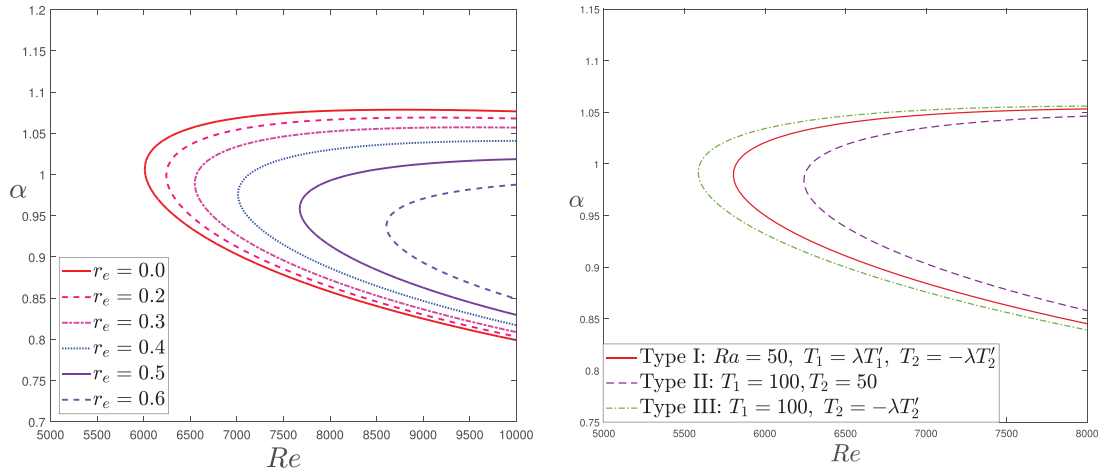

FIG. 6. Neutral stability curves in $Re - \alpha$ plane (where growth rate $\omega_i = 0$): (a) depicting the influence of uniform cross-flow for Type-II configuration with $T_1 = T_2 = 100$; (b) comparison of the results for fixed wall temperature (Type-II) configuration and with that of thermal slippage walls (Types-I, III) when $r_e = 0.4$, $\beta = 0.005$ and $\lambda = 0.2$.

variation, as mentioned in subsection 1 of the Appendix. The behaviors of the eigenvalue spectrum, eigenfunctions of excited eigenmodes, the growth rate of unstable modes, and marginal stability boundaries for various flow parameters are explored numerically. Furthermore, the energy balance is analyzed in Sec. IV A illustrating the impact of various imposed conditions on the above system.

The neutral stability curves in Figs. 6(a) and 6(b), where cross-flow is present but no thermal slip, are also in agreement with the patterns in Sheppard[8] and Fransson and Alfredsson.[5] Figure 6(a) shows the neutral stability curves for Type-II when the temperature of both walls is equally set with variations in cross-flow. An increase in the cross-flow delays the onset of instability as the critical Reynolds number R_c increases, and the size of unstable region shrinks along with reduction in the range of unstable wavenumbers. Therefore, cross-flow stabilizes the flow system, due to the change in shear rate near the walls as well as decay of the flow speed by the presence of vertical cross-flow. Figure 6(b) presents the comparison between the results for Types-I, II, and III of temperature boundary conditions. It is observed that for the same values of flow parameters r_e, β, λ, and Ra and the same initial temperatures of the lower wall, Type-II model is stable for a wider range of Reynolds numbers with a substantial increase in the critical Reynolds number as compared to Type-III model. Furthermore, the stable region in Type-I model is dependent on Rayleigh number, a variation in which can result in a critical Reynolds number higher and lower than that in the Type-II and Type-III models, respectively.

The normalized eigenfunctions for the Orr–Sommerfeld and energy system [Eqs. (22) and (23)], corresponding to the highlighted eigenvalues from Fig. 5(a) are depicted in Fig. 7. The solid line represents the magnitude of the eigenfunction, and the dashed and dotted lines represent the corresponding real and imaginary parts. The $A-$branch mode (Orr–Sommerfeld mode) has minimum variation near the channel walls, and a peak arises near the centerline ($y = 0$) similar to standard channel flow.[30] However, asymmetry is introduced due to the presence of uniform cross-flow across the channel as the

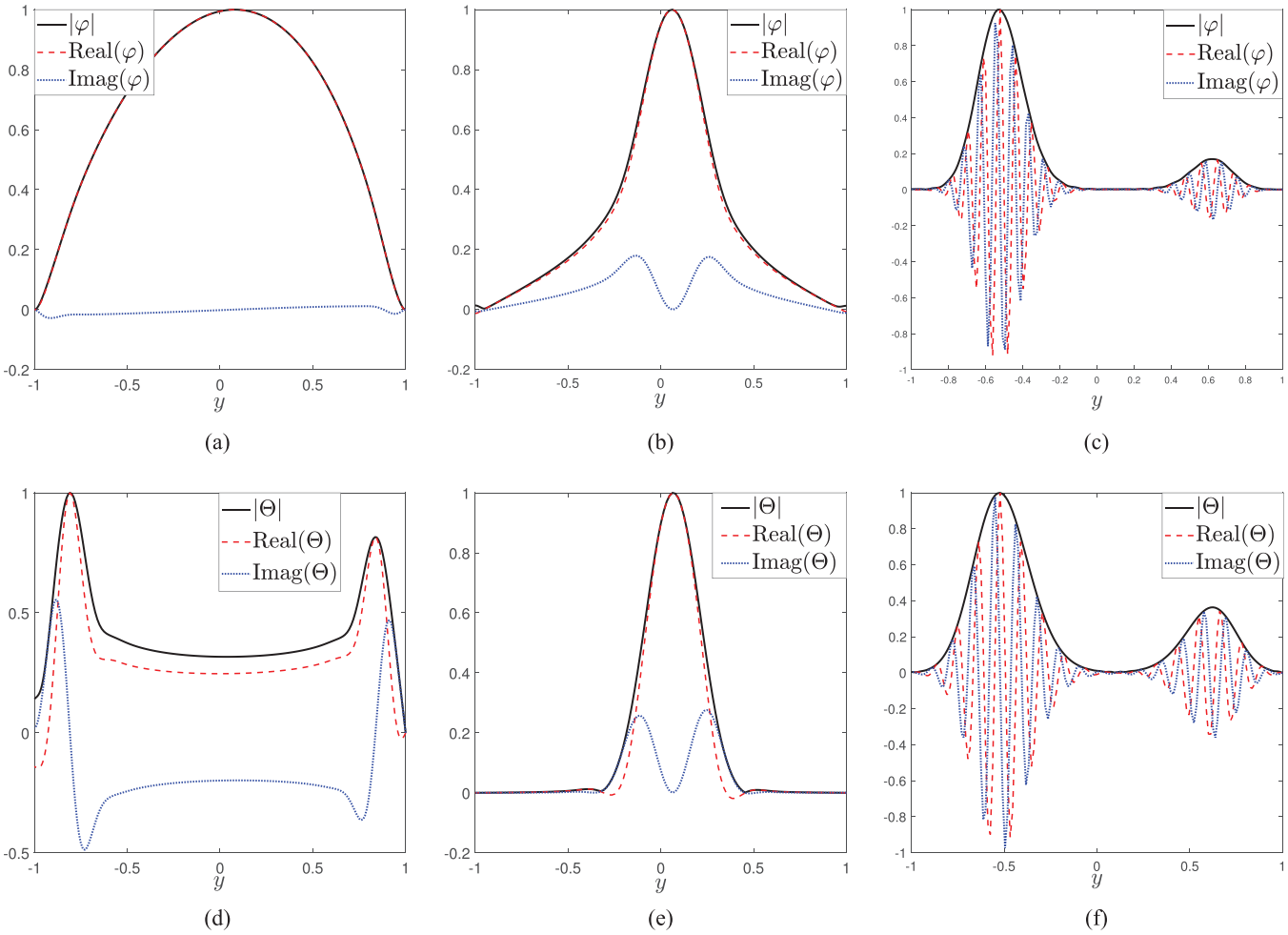

FIG. 7. [(a)–(c)] Orr–Sommerfeld eigenfunctions; [(d)–(f)] temperature eigenfunctions for plane Poiseuille flow with cross-flow and internal heat generation when $Re = 10\,000$, $Ra = 100$, $r_e = 0.4$ and $\lambda = 0.2$. (a) *A*-branch mode. (b) *P*-branch mode. (c) *S*-branch mode.

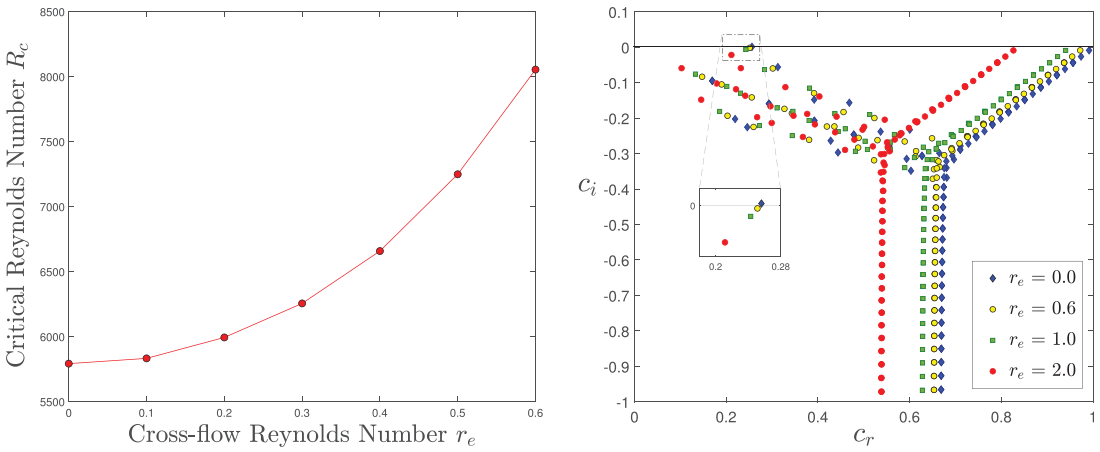

FIG. 8. (a) Variation in critical Reynolds number R_c as a function of cross-flow Reynolds number r_e and (b) influence of r_e on the unstable mode present in $A-$ branch. The wall temperatures are fixed at $T_1 = T_2 = 0$ and $Re = 10\,000$.

maximum is shifted slightly from the centerline [Fig. 7(a)]. In contrast, the mode sourced from the energy equation corresponding to $A-$ branch mode peaks sharply near the walls and falls to a nearly constant lower value in between [Fig. 7(d)]. Both the velocity and temperature eigenfunctions, corresponding to the $P-$ branch, peak around the centerline with minimal variation near the walls, as in Figs. 7(b) and 7(e). Generally, the $S-$ branch modes are highly damped, and the corresponding eigenfunction has a symmetric pattern across the channel centerline.[30] Nevertheless, as per Figs. 7(c) and 7(f), the cross-flow induces asymmetry in the eigenfunctions related to $S-$ mode across $y = 0$, with oscillations being damped near cross-flow exit wall.

Figure 8(a) demonstrates the effect of cross-flow on the critical Reynolds number R_c, which is observed to be highly sensitive to the Reynolds number based on cross-flow (r_e), and the perturbed flow remaining stable over a more significant range of Reynolds numbers for higher r_e, which is analogous to Sheppard.[8] Further details about the eigenvalue spectra are in Fig. 8(b), showing the spectra for different amounts of cross-flows with the same wall temperature, wavenumber $\alpha = 1.0$, and Reynolds number $Re = 10\,000$. Additionally, suppression of the unstable mode is visualized (in the inset figure) for increasing cross-flow parameter r_e.

The isolines of horizontal and vertical components of the velocity perturbations and temperature isotherms are drawn in Figs. 9(a), 9(b), and 9(c), respectively, for the Poiseuille flow having cross-flow, heat influx and outflux along with internal heat generation together with velocity and thermal slips. These results are similar to those in Bajaj.[13] The horizontal velocity perturbations are extremized near the boundaries while the horizontal perturbation is relatively stationary near the centerline. It is also observed that isolines of the vertical velocity perturbations tilt at the boundaries, and this allows the perturbation to access energy from the mean flow.[46] The temperature perturbations follow the energy distributed by the

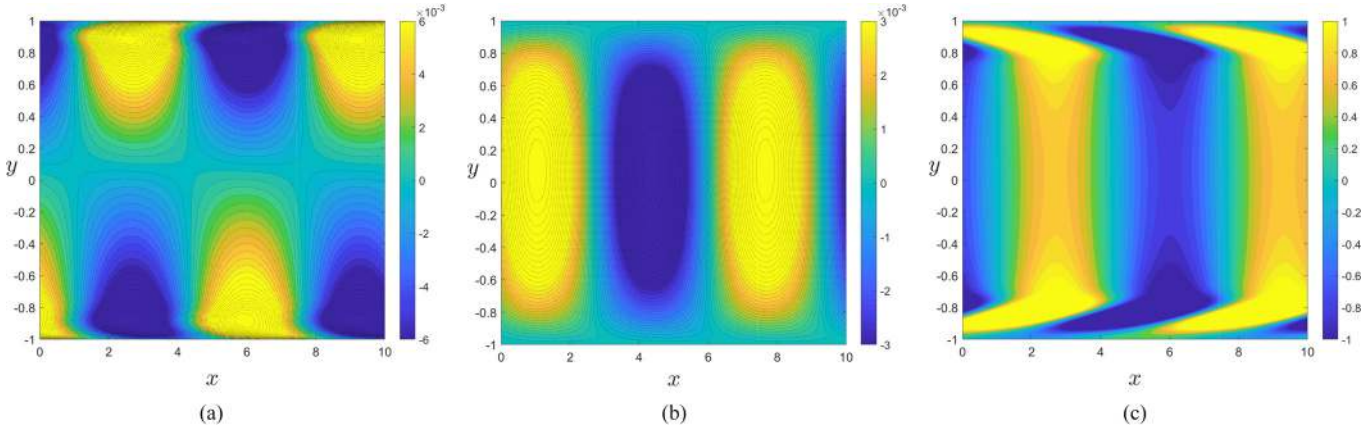

FIG. 9. [(a) and (b)] Velocity isolines and (c) temperature isotherms for the plane Poiseuille flow with velocity slip, uniform cross-flow and internal heat generation when $Re = 10\,000$, $Ra = 100$, $\beta = 0.005$, $r_e = 0.4$ and $\lambda = 0.2$. (a) Horizontal velocity. (b) Vertical velocity. (c) Temperature.

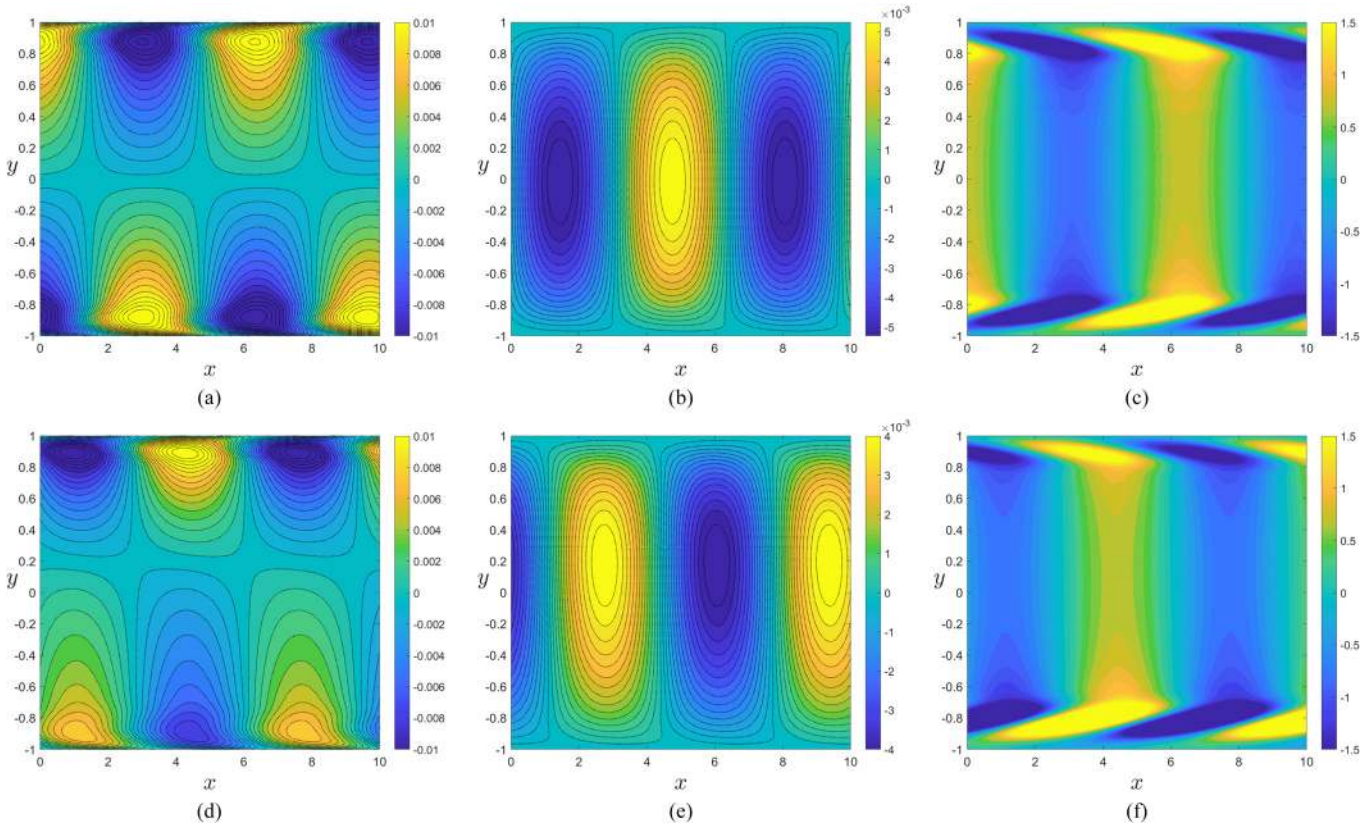

FIG. 10. [(a) and (d)] Horizontal velocity isolines; [(b) and (e)] vertical velocity isolines; [(c) and (f)] temperature isotherms for plane poiseuille flow with velocity slip and internal heat generation when $Re = 10\,000$, $Ra = 100$, $\beta = 0.005$ and $\lambda = 0.2$ with different cross-flows. (a) $r_e = 0.0$. (b) $r_e = 0.0$. (c) $r_e = 0.0$. (d) $r_e = 1.0$. (e) $r_e = 1.0$. (f) $r_e = 1.0$.

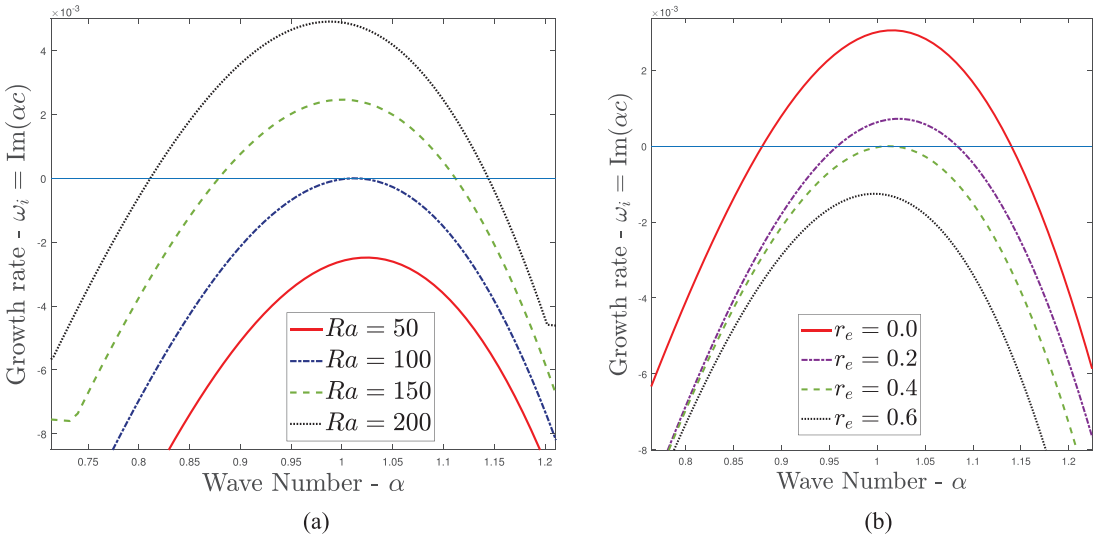

FIG. 11. Growth rate dispersion curves for Type-I flow configuration with different values of (a) Rayleigh number Ra when $r_e = 0.4$ and (b) cross-flow Reynolds number r_e when $Ra = 100$. The other common parameters are $Re = 4267.5$, $\beta = 0.005$ and $\lambda = 0.2$.

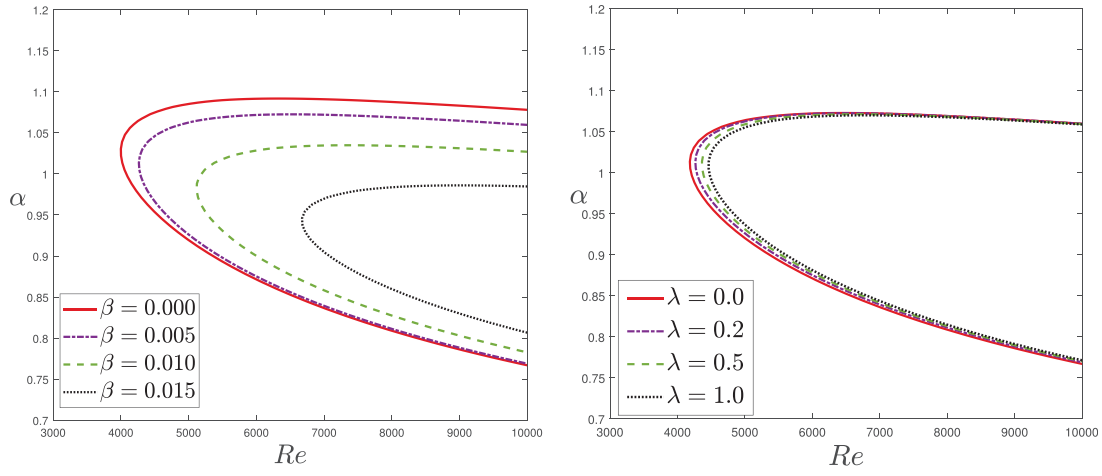

FIG. 12. Neutral stability curves in $Re - \alpha$ plane for varied: (a) velocity slip coefficient (β) with $\lambda = 0.2$ and (b) thermal slip coefficient (λ) with $\beta = 0.005$. The other parameters are $r_e = 0.4$ and $Ra = 100$.

velocity perturbations, as in Fig. 9(b), with maximum perturbation near the boundary walls.

Figure 10 compares velocity and temperature perturbations with and without cross-flow; $r_e = 0.0$ for panels 10(a)–10(c) and $r_e = 1.0$ for panels 10(d)–10(f). The minimum of horizontal and maximum of vertical velocity perturbations are shifted in the direction of the cross-flow, while the density of temperature perturbations decrease near the cross-flow exit wall which is congruent with the consequences of Bajaj.[13]

Section IV A elaborates on the results for various types of flow configurations with different thermal boundary conditions in a more sophisticated way.

Type-I: Flow with internal heat source and thermal slip at the channel walls: Figure 11(a) depicts growth rates for the extreme excited mode of the disturbed flow in the presence of internal heat generation for various Ra when $Re = 4267.5, r_e = 0.4, \lambda = 0.2$. The flow is observed to destabilize for values of $Ra \geq 100$ and $\omega_i > 0$ for certain range of α. Figure 11(b) plots the growth rates illustrating the influence of cross-flow Reynolds number r_e on the fluid flow with internal heat generation. It is observed that an increase in the Rayleigh number destabilizes the fluid flow between parallel porous walls, which corresponds to an increase in internal temperature of the fluid. In contrast, for a fixed rate of heat generation and conduction through channel walls, increase in the cross-flow Reynolds number stabilizes the fluid flow by diminishing the temporal growth rate [Fig. 11(b)]. This is consistent with earlier works in the literature. Additionally, in this case, the maximum growth rate becomes zero for the critical Reynolds number $R_c = 4267.5$ with $Ra = 100$.

Figures 12(a) and 12(b), respectively, show the influence of velocity slip and thermal slip coefficients on the marginal stability curves. The flow is observed to stabilize due to an increase in either the velocity slip coefficient or the thermal slip coefficient. The changes in the value of the velocity slip coefficient result in a significant reduction in the area of the unstable region, and the flow is highly sensitive to small variations in the value of the velocity slip coefficient resulting in significant increases in the critical Reynolds number. Figure 12(b) illustrates that the flow is not very sensitive to the thermal slip coefficient λ, as a significant change in λ results in small variation of the critical Reynolds number and the set of unstable wavenumbers. However, an increase in λ has a stabilizing effect on the flow by increasing the critical Reynolds number.

Type-II: Flow without internal heat source and constant wall temperature: In this configuration, the heat source is excluded and the walls of the channel are such that there is no temperature slip. Having a temperature gradient between the channel walls ($T_1 = 300, T_2$ is varied) with a particular r_e ($r_e = 0.4$) and Re ($Re = 7000$), the increasing temperature difference between the walls destabilizes the flow by rising the maximum growth rate and widening the range of unstable wavenumbers in the dispersion curves [Fig. 13(a)]. Note that, for the considered parameters, the temperature gradient is decreasing in the direction of the cross-flow, and the lower wall at $y = -1$ has a higher temperature. Hence, the current results are consistent with the classical Rayleigh–Benard instability mechanism. However, it is observed that increasing the cross-flow Reynolds number suppresses the flow instability [Fig. 13(b)]. Conclusively, a minimal temperature difference between the walls or a high upward cross-flow velocity favors the flow stability in this case. Furthermore, the typical neutral stability curves are plotted in Figs. 13(c) and 13(d) for a clear understanding and the results follow similar conclusions as Figs. 13(a) and 13(b). The negative r_e in Fig. 13(d) suggests a downward cross-flow and it alters the effect upon flow stability.

Type-III: Flow with a fixed temperature at one wall and thermal slip on the other wall: In Figs. 14 and 15, the plots of neutral stability curves demonstrate the effect of various physical parameters on the stability of the channel flow for Type-III thermal boundary conditions. From Figs. 14(a) and 14(b), the high values of velocity slip (β) or the smaller values of lower plate temperature (T_0) are observed to stabilize the fluid flow. A significant increase in the critical Reynolds number and a narrower unstable wavenumber range are noticed upon increase in β or decrease in T_0.

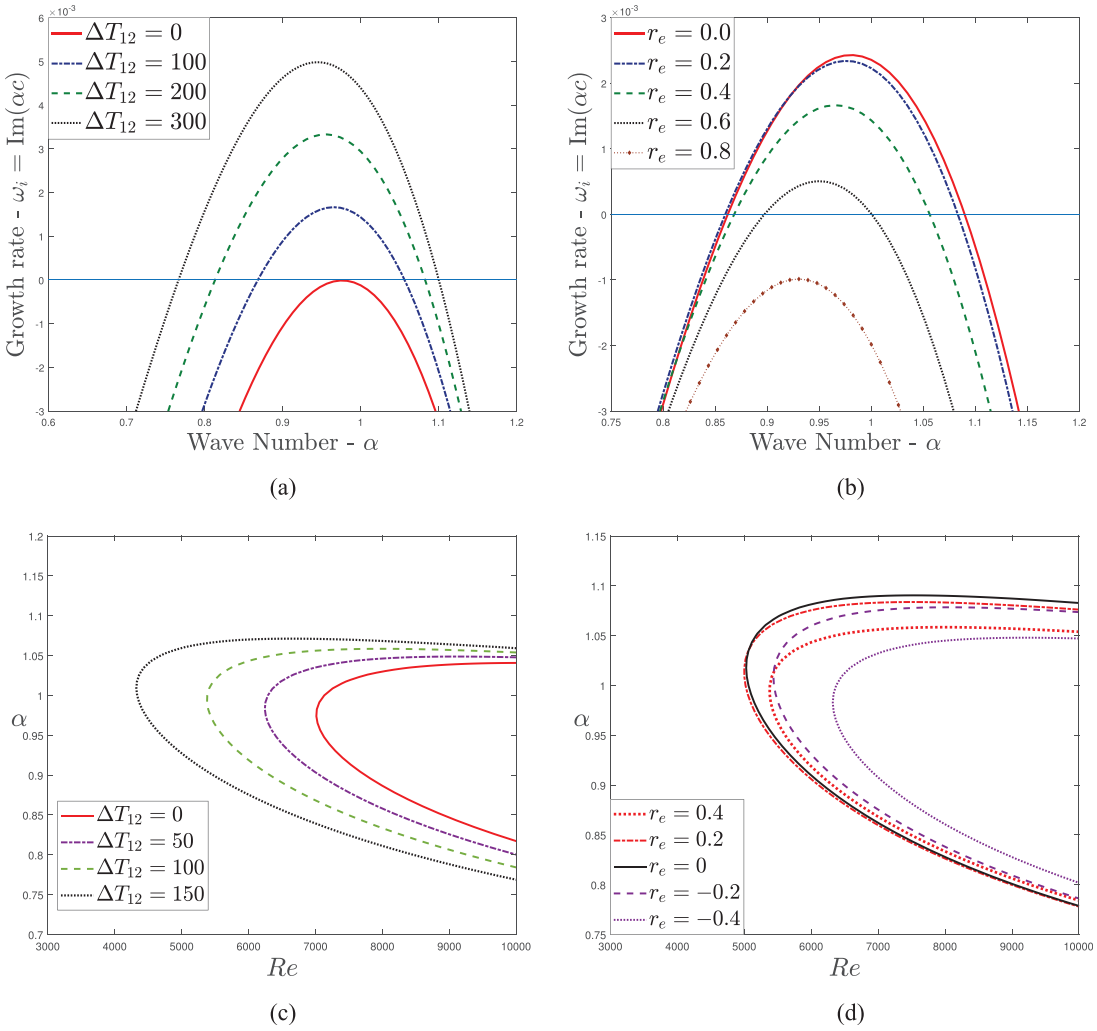

FIG. 13. Results for the Type-II configuration with different values of: [(a) and (c)] the temperature difference $\Delta T_{12} = (T_1 - T_2)$ between the walls with $T_1 = 300$ (T_2 varied), $r_e = 0.4$, $\beta = 0.005$; and [(b) and (d)] the cross-flow Reynolds number with $T_1 = 300$, $T_2 = 200$, $\beta = 0.005$. In the subfigures [(a) and (b)] the growth rate dispersion curves are drown with $Re = 7000$ and the neutral stability curves are plotted in [(c) and (d)].

Additionally, the marginal stability boundaries are plotted in Fig. 15 to check the influences of r_e and λ for a particular value of temperature at the lower wall (i.e., at $T_0 = 100$). Its seen that increasing cross-flow Reynolds number r_e has a stabilizing effect on the flow, and the critical Reynolds number for instability increases as r_e is increased [Fig. 15(a)]. More significantly, an increase in the value of thermal slip on the upper wall ($y = +H$) stabilizes the flow owing to the increase in the critical Reynolds number and decrease in the area of the unstable region [Fig. 15(b)].

A. Energy distribution analysis

In this subsection, the energy fluctuation inside the perturbed flow system corresponding to various energy terms as described in Eq. (30) is analyzed. The comparisons with growth rate for linear instability can be easily applied, as the disturbance kinetic energy (*DKE*) of the flow system is proportional to the temporal growth rate of perturbations, and the stability or instability is characterized by $DKE < 0$ or $DKE > 0$. Further, as the viscous dissipation energy (VDE) is always negative ($VDE < 0$),[42] hence, the energy needed for the growth of small initial disturbances must be extracted from either the Reynolds stress (*BReS*) or the cross-flow (*CReS*)/thermal effects (*TIE*) or consolidate. Figure 16 illustrates the accuracy of the energy computation by comparing the growth rates corresponding to the Orr–Sommerfeld analysis and the Reynolds–Orr energy method. It may be noted that the evaluated growth rate via either methods is in excellent agreement and are numerically equal up to five decimal places.

The results discussed in Figs. 17–20 establish the base flow and the thermal effects at the boundaries as leading mechanisms that drive the instability in the considered flow system. In comparison to these phenomena, the cross-flow has a weaker effect on the energy transfer into the perturbed flow, as order of magnitude of *CReS* is very inferior

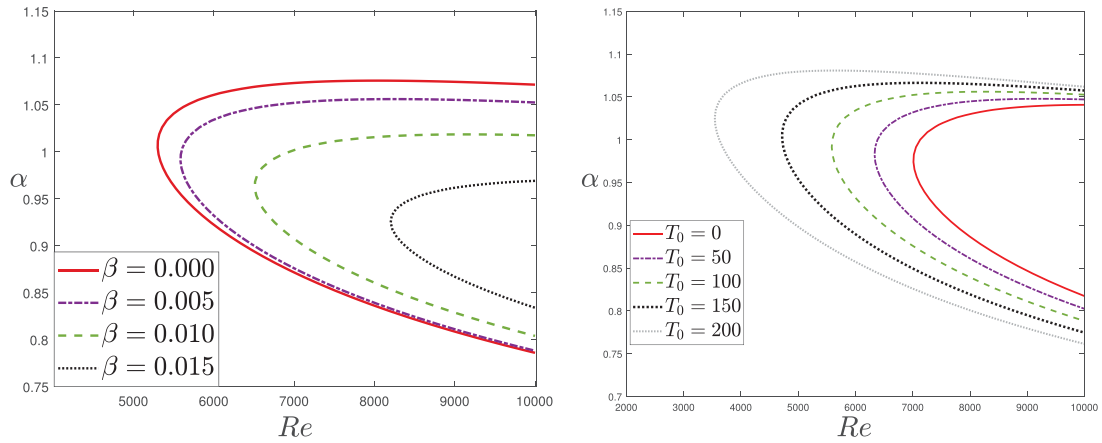

FIG. 14. Neutral stability curves for Type-III with different values of (a) wall velocity slip β, when $T_0 = 100$, $\lambda = 0.2$, $r_e = 0.4$ and (b) the lower wall temperature (T_0), when $\beta = 0.005$, $\lambda = 0.2$ and $r_e = 0.4$.

to that of both *BRes* and *TIE*. Moreover, as argued in Kelly *et al.*,[40] the analysis implementing a crude base velocity at high Reynolds numbers, whereby viscous effects are negligible, but exact boundary conditions at the channel walls are successful in describing such instability. Thus, for unstable wavenumbers, depicted earlier in Sec. IV, $DKE > 0$ in Eq. (30) implies that the small initial disturbances grow due to increase of the Reynolds stress and thermally induced energies. Whereas for stable wavenumbers, more energy is dissipated from the flow than transferred into the flow, i.e., $|VDE| > |BReS + CReS + TIE|$, which also corresponds to the negative rate of kinetic energies of the perturbations.

Figures 17 and 18 plot the energy components of Eq. (30) as the function of wavenumber α for different values of cross-flow Reynolds number r_e corresponding to the unstable region in Figs. 11 and 13, respectively. In both figures, it is observed that as r_e is increased, even though *CReS* and *TIE* increase, Reynolds stress *BReS* decreases, and magnitude of viscous dissipation $|VDE|$ also increases. Consequently, the flow stabilizes upon increasing the cross-flow speed, as the effects of energy transfer into the flow via cross-flow and thermal effects are negated by the antithetical influence of Reynolds stress and viscous dissipation which are larger in magnitude.

Variations of energy terms as the function of wavenumber α are plotted in Figs. 19 and 20 corresponding to Type-III configuration. These figures aim to illustrate the energy sources responsible for the instabilities which are noticed in Fig. 14 for different values of velocity

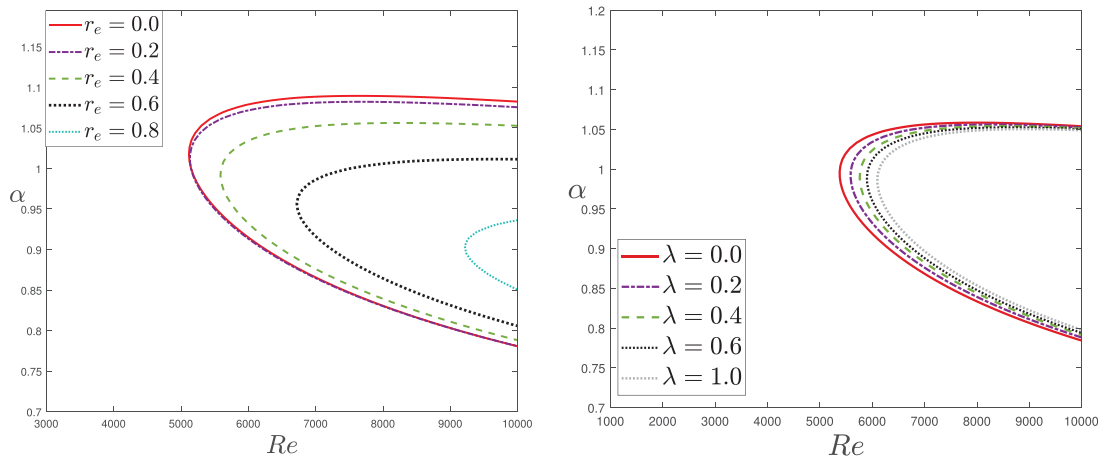

FIG. 15. Neutral stability curves for the Type-III configuration with $T_0 = 100$, having different values of (a) cross-flow Reynolds number (r_e) with $\lambda = 0.2$ and (b) thermal slip parameter (λ) with $r_e = 0.4$.

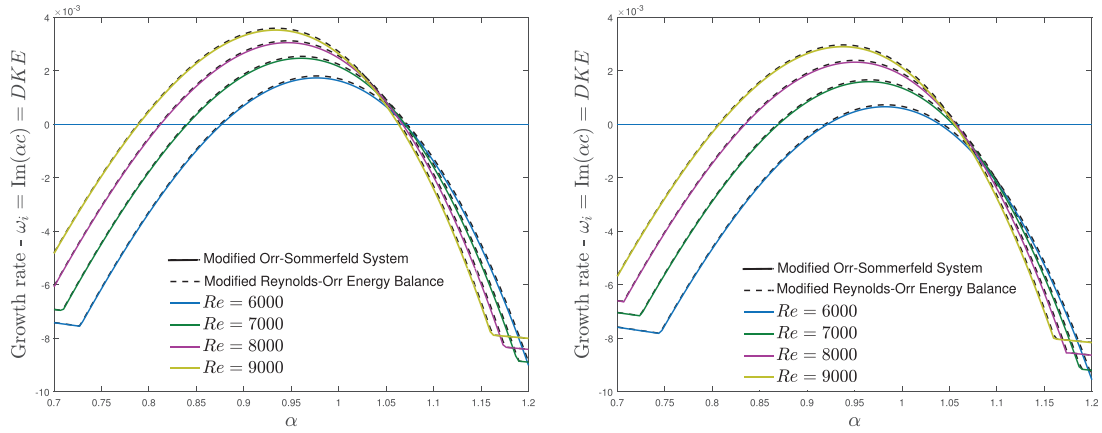

FIG. 16. Growth rate comparison corresponding to the Orr–Sommerfeld system and Reynolds–Orr energy analysis: (a) Type-I with $Ra = 100$, and (b) Type-II with $T_1 = 300$, $T_2 = 200$. The other parameters are $r_e = 0.4$, $\beta = 0.005$ and $\lambda = 0.2$.

slip β and in Fig. 15 for different values of thermal slip λ. It is observed that as β is (Fig. 19), the Reynolds stress diminishes, which restricts the energy transfer from the base flow to perturbed flow and damping the change n kinetic energy. The same is also induced by the increase in viscous dissipation (*VDE*) throughout the selected wavenumber regime and the flow stabilizes with stronger wall velocity slip (β).

Further, an increase in β has a negligible energy damping effect on *TIE* as well, and while the effect on *CReS* is substantial, the relative magnitude is contemptible to have any authentic influence on overall kinetic energy. Results in Fig. 20 suggest that an increase in the thermal slip λ dampens the Reynolds stress as well as energy contribution from the thermal effects (*TIE*) to stabilize the overall flow. Further, it boosts the viscous dissipation slightly and diminishes the cross-flow energy term (*CReS*); however, the magnitude is very small to have any effect on overall energy balance

V. CONCLUSIONS

The work explores the linear stability characteristics of a plane Poiseuille flow modified with uniform cross-flow and a temperature gradient between the channel walls having small permeability. The temperature gradient is the result of the wall temperature difference and/or the internal heat generation inside the flow. The two-

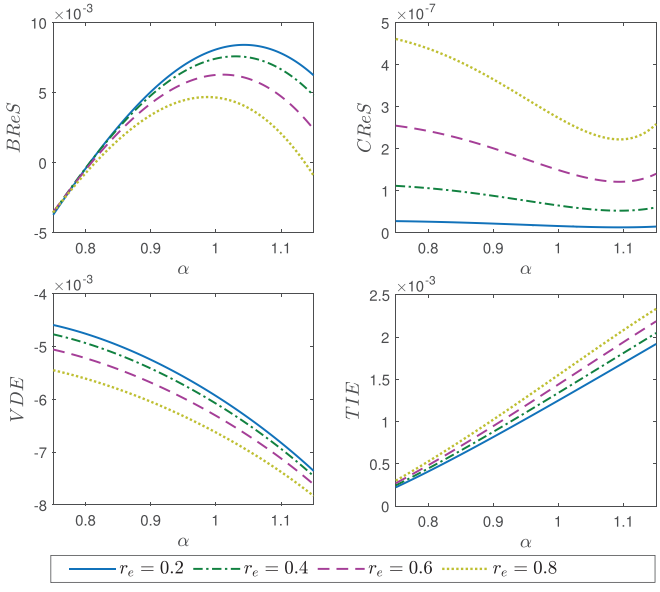

FIG. 17. Effect of cross-flow on energy terms for Type-I flow configuration with $Ra = 100$, $Re = 4627.5$, $\beta = 0.005$ and $\lambda = 0.2$.

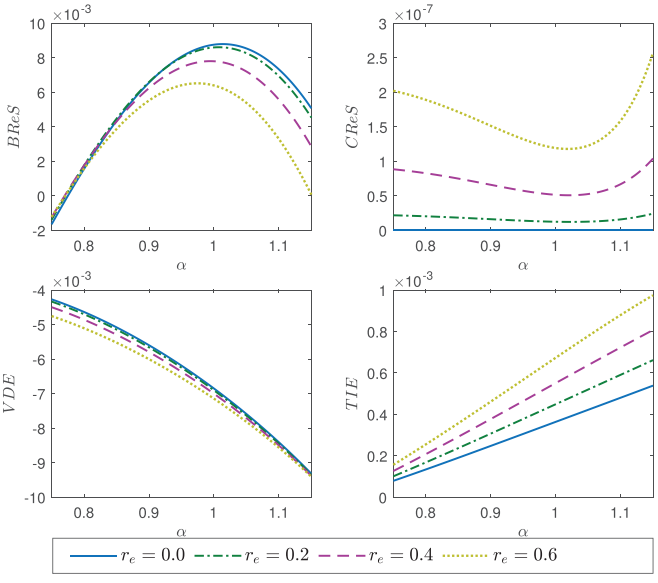

FIG. 18. Effect of cross-flow on energy terms for Type-II flow configuration with $T_1 = 300$, $T_2 = 200$, $Re = 7000$, $\beta = 0.005$ and $\lambda = 0.2$.

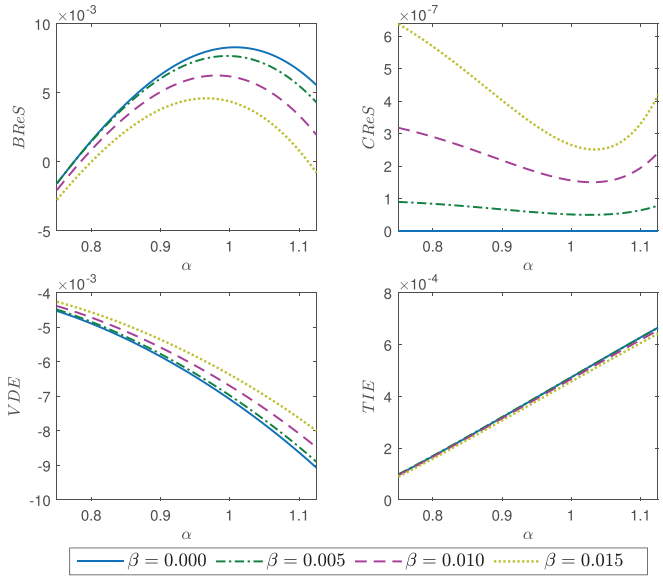

FIG. 19. Effect of velocity slip on energy terms for Type-III flow configuration with $T_1 = 100$, $r_e = 0.4$, $Re = 7000$ and $\lambda = 0.2$.

dimensional model of the flow is studied for three different scenarios, including the boundary slip or jump at the porous channel walls. A modified Orr–Sommerfeld and energy equations system is derived and thereby solved numerically to trigger out the instabilities for each configuration; characterized by the Reynolds, cross-flow Reynolds, and Rayleigh numbers together with the velocity and thermal slip. The temporal growth rate curves and the neutral stability boundaries corresponding to the disturbances are portrayed using the most unstable eigenmode of the system, which provides the range of critical parameters for temporal instability. The corresponding eigenfunctions of the unstable eigenmode are also captured to know the possible mechanism of the instability. Furthermore, the results are consolidated with an energy balance analysis of the given model by deriving a modified Reynolds–Orr Energy equation and exploring the energy changes, leading a cohesive understanding of the instability of the flow system.

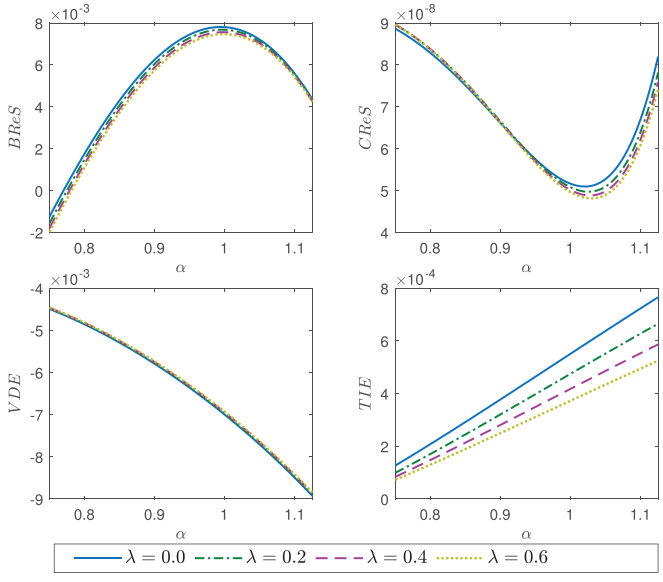

FIG. 20. Effect of thermal slip on energy terms for Type-III flow configuration with $T_1 = 100$, $r_e = 0.4$, $Re = 7000$ and $\beta = 0.005$.

The first configuration combines the uniform internal heat generation with the heat source and sink at the channel walls. Subsequently, a convenient thermal slip boundary condition models the thermal variation at the walls. Numerical results with this configuration suggest that, an increase in upward cross-flow velocity or a decrease in the internal heat generation inside the flow act as stabilizing factors (Figs. 6, 8, and 11). It is illustrated by the suppression of the unstable eigenmodes at various wavenumbers (Fig. 8) for higher r_e and lower Ra, along with the temporal decay of the most unstable mode and reduction of the marginal stability boundaries. Further, the velocity and temperature slip have stabilizing influence.

In the second scenario, the internal heat source is absent, and the channel walls are kept at a constant temperature (not necessarily equal). The stability of flow system is generally exacerbated by the increase in the Reynolds number and the temperature difference between the walls [Fig. 13]. Whereas, the stronger cross-flow velocity in terms of larger r_e has stabilizing effect. It is to be noted that in the absence of cross-flow ($r_e = 0$), the result of the current study tally with those of the classical Poiseuille–Rayleigh–Bénard instability.

Under the third aspect, one of the channel walls has a temperature jump and is modeled with the thermal slip, and the opposite wall fosters an uniform constant temperature. Consequently, for a constant temperature at the lower wall and the freely conducting upper wall, when the lower wall temperature increases the configuration becomes a more unstable thermal stratification [Fig. 14(b)]. However, the upward cross-flow velocity and the thermal slip at the upper wall has a reverse effect and stabilizes the flow [Figs. 15(a) and 15(b)]. Additionally, the wall velocity slip pushes to stabilize the flow by changing the wall shear rate of the flow system [Fig. 14(a)].

An energy budget analysis is done to understand the underlying instability mechanisms for all three types of configurations. It is observed that the energy transferred from the base flow to the perturbed flow and the energy sourcing from the cross-flow as well as thermal effect are responsible for the linear instability in the perturbed system. Further, the wall velocity slip and thermal slip at the walls control the energy fluctuation from all the sources.

Conclusively, on comparison of the flow configuration with zero temperature gradient (zero or equal wall temperatures), the flow with different wall temperatures and/or internal heating is more unstable. The upward cross-flow always has stabilizing influence. The Poiseuille–Rayleigh–Bénard instability can be suppressed using velocity and thermal slip at the channel walls. The current study provides a versatile array of passive control mechanisms for wall-bounded flows.

ACKNOWLEDGMENTS

H.B. and S.G. gratefully acknowledge the financial support from SERB, Department of Science and Technology, Government of India through "CRG" project, Award No. CRG/2018/004521.

The authors report no conflict of interest.

APPENDIX: PROCEDURE OF BASE-FLOW SOLUTIONS

The nondimensional base flow governing equations can be obtained from the Navier–Stokes equations (9)–(12) after assuming that the mean flow is unidirectional, fully developed, and locally parallel as

$$-\partial_x P_b + \partial_{yy} U_b = ReV_0\, \partial_y U_b, \tag{A1}$$

$$-\partial_y P_b + T_b = 0, \tag{A2}$$

$$\partial_{yy} T_b - r_e \partial_y T_b = -Ra, \tag{A3}$$

where, P_b and T_b are base pressure and temperature, respectively. Note that, the solution of Eq. (A3) will provide the base temperature profile T_b, and it is assumed that there is no or negligible variation of base temperature in the streamwise direction. Once $T_b(y)$ is known, the base pressure P_b can be derived from Eq. (A2). Whereas the base velocity component U_b is the solution of Eq. (A1). Moreover, $ReV_0 = r_e$ and the velocity boundary conditions contain the parameter β thus the base velocity profile depends on r_e and β.

Further, a constant pressure gradient acts in the streamwise direction and drives the fluid flow with base velocity profile $U_b(y)$, and the temperature gradient between the two walls maintains the mean temperature profile $T_b(y)$. As a consequence, the pressure gradient $\partial_x P_b = -P_0$ is fixed and for the case of Poiseuille type channel flow, it is a usual assumption. Furthermore, Eq. (A1) gives the solution for the base velocity $U_b(y)$ that is independent of the x coordinate.

1. Base temperature profiles

Following the standard procedure in conjunction with the earlier literature[5,8,30] and using the base/equilibrium flow assumptions, the equation for the base temperature (T_b),

$$\partial_{yy} T_b - r_e \partial_y T_b + Ra = 0 \tag{A4}$$

is derived from the energy equation (12). Clearly, Eq. (A4) as well as the boundary conditions for temperature are only dependent on the variable y. Considering no or negligible variation of base temperature with respect to x, the solution T_b of Eq. (A4) is a function of y alone. According to the formulation of the problem, the channel walls are maintained with constant uniform temperature along $x-$ direction, and there is a volumetric uniform heat source with constant strength $\mathcal{Q}$ inside the flow domain. The Rayleigh number Ra is the nondimensional form of uniform internal heating $\mathcal{Q}$. Here, the effect of internal heating taken into account and so, the base temperature (T_b) given in Eq. (17) contains the Rayleigh number Ra and the T_b profile changes with different Ra (see Fig. 3).

2. Base velocity profile

The equation for the base velocity [Eq. (A1)] contains the base pressure gradient with respect to x ($\partial_x P_b$). Whereas Eq. (A2) together with the condition $\partial_x P_b = -P_0$ and T_b from Eq. (A3) gives the expression for the base pressure $P_b(x, y)$. Thus, first, the following two equations are used to obtain the base pressure profile:

$$-\partial_y P_b + T_b = 0, \tag{A5}$$

$$-\partial_x P_b = P_0. \tag{A6}$$

Integrating Eq. (A5) with respect to y, one can write

$$P_b = \int T_b(y)dy = g(y) + f(x) + c, \tag{A7}$$

where f and g are only function of x and y, respectively, and c is a constant. Such a form of the P_b is possible because T_b is a function of y alone. Putting the above P_b in Eq. (A6),

$$\frac{df}{dx} = -P_0, \tag{A8}$$

which implies $f(x)$ is a linear function of x and thus T_b also linearly dependent on x. Moreover, we can express the base pressure as

$$P_b(x, y) = \int T_b(y)dy - P_0 x = c + g(y) - P_0 x. \tag{A9}$$

In the current study, a constant pressure gradient in the x-direction drives the flow, hence its clear that the gradient $\frac{\partial P_b}{\partial x}$ will not be a function of y. Finally, using the velocity boundary conditions, the streamwise base velocity (U_b) can be obtained explicitly as given in Eq. (16).

DATA AVAILABILITY

The data that supports the findings of this study are available within the article, highlighted in each of the figure captions and corresponding discussions.

REFERENCES

[1] C. Wang, "Thin film flowing down a curved surface," Z. Angew. Math. Phys. **35**, 532–544 (1984).
[2] T. Weisshaar, "Aerospace structures—An introduction to fundamental problems, Course Notes" (Purdue University, West Lafayette, 2011).
[3] W. O. Criminale, T. L. Jackson, and R. D. Joslin, *Theory and Computation in Hydrodynamic Stability* (Cambridge University Press, 2018).
[4] D. J. Tritton, *Physical Fluid Dynamics* (Springer Science and Business Media, 2012).
[5] J. H. Fransson and P. H. Alfredsson, "On the hydrodynamic stability of channel flow with cross flow," Phys. Fluids **15**, 436–441 (2003).
[6] J.-J. Shu, J. B. M. Teo, and W. K. Chan, "Fluid velocity slip and temperature jump at a solid surface," Appl. Mech. Rev. **69**, 020801 (2017).
[7] F. Hains, "Stability of plane Couette-Poiseuille flow with uniform crossflow," Phys. Fluids **14**, 1620–1623 (1971).
[8] D. M. Sheppard, "Hydrodynamic stability of the flow between parallel porous walls," Phys. Fluids **15**, 241–244 (1972).
[9] M. C. Potter and E. Graber, "Stability of plane Poiseuille flow with heat transfer," Phys. Fluids **15**, 387–391 (1972).
[10] Y.-Q. Liu and K.-Q. Zhu, "Study of shear-thinning/thickening effects on plane Couette-Poiseuille flow with uniform crossflow," Appl. Math. Mech. **35**, 549–566 (2014).
[11] H. C. Chu, S. Garoff, T. M. Przybycien, R. D. Tilton, and A. S. Khair, "Dispersion in steady and time-oscillatory two-dimensional flows through a parallel-plate channel," Phys. Fluids **31**, 022007 (2019).
[12] A. Guha and I. A. Frigaard, "On the stability of plane Couette–Poiseuille flow with uniform crossflow," J. Fluid Mech. **656**, 417–447 (2010).
[13] R. Bajaj, "The stability of the heated plane poiseuille flow subjected to a uniform crossflow," Int. J. Non-Linear Mech. **77**, 232–239 (2015).
[14] S. Sharma, D. K. Maiti, M. M. Alam, and B. K. Sharma, "Nanofluid flow and heat transfer from heated square cylinder in the presence of upstream rectangular cylinder under Couette-Poiseuille flow," Wind Struct. **29**, 65–75 (2019).
[15] S. Santra, S. Das, and S. Chakraborty, "Electric field-induced pinch-off of a compound droplet in Poiseuille flow," Phys. Fluids **31**, 062004 (2019).

[16]X. Nicolas, A. Mojtabi, and J. K. Platten, "Two-dimensional numerical analysis of the Poiseuille–Bénard flow in a rectangular channel heated from below," Phys. Fluids **9**, 337–348 (1997).
[17]K. Gage and W. Reid, "The stability of thermally stratified plane Poiseuille flow," J. Fluid Mech. **33**, 21–32 (1968).
[18]A. Sameen and R. Govindarajan, "The effect of wall heating on instability of channel flow," J. Fluid Mech. **577**, 417–442 (2007).
[19]S. Özgen, Z. Dursunkaya, and A. A. Ebrinç, "Heat transfer effects on the stability of low speed plane Couette-Poiseuille flow," Heat Mass Transfer **43**, 1317–1328 (2007).
[20]A. Barletta and D. Nield, "On the Rayleigh–Bénard–Poiseuille problem with internal heat generation," Int. J. Therm. Sci. **57**, 1–16 (2012).
[21]D. Nield and A. Barletta, "Thermal instability in a plane channel with internal heating and horizontal Poiseuille throughflow," Int. J. Heat Mass Transfer **55**, 1095–1102 (2012).
[22]S. Yao, T. Fang, and Y. Zhong, "Heat transfer of a generalized stretching/shrinking wall problem with convective boundary conditions," Commun. Nonlinear Sci. Numer. Simul. **16**, 752–760 (2011).
[23]M. Sahraoui and M. Kaviany, "Slip and no-slip temperature boundary conditions at the interface of porous, plain media: Convection," Int. J. Heat Mass Transfer **37**, 1029–1044 (1994).
[24]K. Cao and J. Baker, "Slip effects on mixed convective flow and heat transfer from a vertical plate," Int. J. Heat Mass Transfer **52**, 3829–3841 (2009).
[25]S. Mukhopadhyay, "Effects of slip on unsteady mixed convective flow and heat transfer past a stretching surface," Chin. Phys. Lett. **27**, 124401 (2010).
[26]L. Crane and A. McVeigh, "Accelerated slip flow past a cylinder," Z. Angew. Math. Phys. **62**, 365–376 (2011).
[27]C. Chai and B. Song, "Stability of slip channel flow revisited," Phys. Fluids **31**, 084105 (2019).
[28]Q.-F. Fu, T. Hu, and L.-J. Yang, "Instability of a weakly viscoelastic film flowing down a heated inclined plane," Phys. Fluids **30**, 084102 (2018).
[29]S. Ghosh, "Relative effects of asymmetry and wall slip on the stability of plane channel flow," Fluids **2**, 66 (2017).
[30]P. J. Schmid, D. S. Henningson, and D. Jankowski, "Stability and transition in shear flows. Applied mathematical sciences, vol. 142," Appl. Mech. Rev. **55**, B57–B59 (2002).
[31]C. Canuto, M. Y. Hussaini, A. Quarteroni, A. Thomas, Jr. *et al.*, *Spectral Methods in Fluid Dynamics* (Springer Science and Business Media, 2012).
[32]S. A. Orszag, "Accurate solution of the Orr–Sommerfeld stability equation," J. Fluid Mech. **50**, 689–703 (1971).
[33]K. Sahu and O. Matar, "Stability of plane channel flow with viscous heating," J. Fluids Eng. **132**, 011202 (2010).
[34]S. Ghosh and R. Usha, "Stability of viscosity stratified flows down an incline: Role of miscibility and wall slip," Phys. Fluids **28**, 104101 (2016).
[35]L.-S. Kuo and P.-H. Chen, "Effects of slip boundary conditions on Rayleigh-Bénard convection," J. Mech. **25**, 205–212 (2009).
[36]P. L. Kapitza, "The study of heat transfer in helium II," J. Phys.-USSR **4**, 181–210 (1941).
[37]D. Nield and A. Kuznetsov, "Forced convection with slip-flow in a channel or duct occupied by a hyper-porous medium saturated by a rarefied gas," Transp. Porous Media **64**, 161–170 (2006).
[38]A. Kuznetsov and D. Nield, "Thermally developing forced convection in a porous medium occupied by a rarefied gas: Parallel plate channel or circular tube with walls at constant heat flux," Transp. Porous Media **76**, 345–362 (2009).
[39]P. Vadi and S. Rizvi, "Experimental evaluation of a uniform transmembrane pressure crossflow microfiltration unit for the concentration of micellar casein from skim milk," J. Membr. Sci. **189**, 69–82 (2001).
[40]R. Kelly, D. Goussis, S. Lin, and F. Hsu, "The mechanism for surface wave instability in film flow down an inclined plane," Phys. Fluids A: Fluid Dyn. **1**, 819–828 (1989).
[41]L. Ren and D. H. Xia, "Generalized Reynolds-Orr energy equation with wall slip," in *Applied Mechanics and Materials* (Trans Tech Publ., 2012), Vol. 117, pp. 674–678.
[42]P. Boomkamp and R. Miesen, "Classification of instabilities in parallel two-phase flow," Int. J. Multiphase Flow **22**, 67–88 (1996).
[43]N. Tilton and L. Cortelezzi, "Linear stability analysis of pressure-driven flows in channels with porous walls," J. Fluid Mech. **604**, 411 (2008).
[44]A. Samanta, "Role of slip on the linear stability of a liquid flow through a porous channel," Phys. Fluids **29**, 094103 (2017).
[45]L. M. Mack, "A numerical study of the temporal eigenvalue spectrum of the Blasius boundary layer," J. Fluid Mech. **73**, 497–520 (1976).
[46]W. D. Smyth and J. R. Carpenter, *Instability in Geophysical Flows* (Cambridge University Press, 2019).